MINISTERE DE L'ENSEIGNEMENT SUPERIEUR
ET DE LA RECHERCHE SCIENTIFIQUE

Felix Houphouet-Boigny university

UNITE DE FORMATION ET DE
RECHERCHE SCIENCES DES
STRUCTURES DE LA MATIERE ET DE
TECHNOLOGIE

RÉPUBLIQUE DE CÔTE D'IVOIRE
UNION - DISCIPLINE - TRAVAIL

Nº: 660

SPONSORED BY THE
Federal Ministry
of Education
and Research

MASTER IN RENEWABLE ENERGY AND CLIMATE CHANGE

SPECIALITY: PRODUCTION AND TECHNOLOGY OF GREEN HYDROGEN

MASTER THESIS:

Subject/Topic:

DEEP LEARNING TO AUTOMATE IMAGE ANALYSIS OF OXYGEN BUBBLE DYNAMICS IN PROTON EXCHANGE MEMBRANE ELECTROLYZERS

Presented on 26th September 2023 by

Keusra Armel GOMPOU

Jury:

Dr. MC. ZAHIRI Pascal	**President**
Dr. FOFANA Daouda	**Examinator**
Dr. MC. KOUA B. Kamenan	**Supervisor**
Prof. Dr. rer. nat. Michael H. Eikerling	**Co-Supervisor**

Academic year 2022-2023

DEDICATION

I dedicate this thesis to:

My father, **Gouet Jean GOMPOU**;

My mother, **Ouanglo Lucie Valentine DETOPEUH**;

My grandmother, **Emilie GNAHE**;

My auntie, **Felicite STANLEY** and ;

My friend, **Yakre Daman Jaures MIAN**.

ACKNOWLEDGEMENTS

First of all, I am really thankful to the **West African Science Service Center on Climate Change and Adapted Land Use** (WASCAL) for giving me the opportunity to be part of this amazing program, as well as the **German Federal Ministry of Education and Research** (BMBF) for their financial support. This scholarship granted to me, actually represents a milestone in my futur carrer.

I would like to deeply thank **Prof. Dr. rer. nat. Michael H. Eikerling**, Chair for Theory and Computation of Energy Materials, Forschungszentrum Juelich GmbH for accepting me in his institute and allowing me to work on a very interesting and high-relevant investigation topic. His attention and hospitality also kept me motivated throughout my internship in your institute.

I would like to express my sincere thanks to **Prof. Rabani Adamou** and **Dr. Kouassi K. Edouard**, directors of WASCAL Niger and WASCAL Cote d'Ivoire respectively, for being with me along the program.

I would like to say many thanks to **Dr. Kourosh Malek**, Division Head for Artificial Materials Intelligence (AMI) at Chair for Theory and Computation of Energy Materials, Forschungzentrum Juelich GmbH for his deep involvement in this work by organizing meeting and check the progress of the work.

My sincere thanks goes to **Dr. Mohammad J. Eslamibidgoli**, Research Associate at Forschungszentrum Juelich GmbH, for supervising this project. He has always been there for me, providing new exciting ideas and relevant materials for this work, as well as helping me to think critically to overcome challenges faced throughout the project.

I would also like to thank **Dr. Kamenan B. Koua**, Graduate Teaching Assistant at the University Felix Houphouet Boigny (UFHB), for supervising the organisation of the thesis document in accordance with the thesis formatting guidelines stipulated by UFHB.

I would like to say thank you to **Dr. Pascal Zahiri**, Graduate Teaching Assistant at the University Felix Houphouet Boigny (UFHB), for presiding my master's thesis defense.

I would like to thank **Dr. Daouda Fofana**, Doctor at the University Felix Houphouet Boigny (UFHB), for thorougthly examining my master's thesis document.

Last but not least, I am infinitely thankful to **Andre C. Granero**, PhD student at Forschungszentrum Juelich GmbH, for being such a good and cool mentor to me. Your insights, comments, empowerments and friendship have been significantly helpful in the progress of this work.

I would like to give a special thanks to **my family**, **my colleagues** at WASCAL and Forschungszentrum Juelich IEK-13, **my friends** in Ghana, Niger and Cote d'Ivoire for the love accorded to my modest person. We will always be together.

I would like to extend my gratitude to the **Gauss Center for Supercomputing** e.V. (www.gauss-centre.eu) for generously supporting this project. The computing time on the GCS Supercomputer **JUWELS** at Jülich Supercomputing Centre (JSC) provided by the John von Neumann Institute for Computing (NIC) has been instrumental in the successful completion of this research.

Finally, I acknowledge the valuable support from the **Helmholtz Imaging Platform**, **HIP**, a component of the Helmholtz Incubator on Information and Data Science, which has significantly contributed to the elaboration of this project.

ABSTRACT

The massive use of fossil fuels due to strong industrialization and exponential population growth is the cause of human-made climate change and its unprecedented devastating environment benign, necessitating an immediate energy transition to renewable energy technologies. In this context, green hydrogen, seen as a fuel and a means of storing energy, represents an important option for an effective energy shift. With the aim of large scale hydrogen production and storage, significant efforts have been made in the field of material science to enable the development of economically viable proton exchange membrane (PEM) electrolyzers.

However, water electrolyzers suffer from performance loss due to the formation and accumulation of oxygen bubbles at the anodic side. Understanding the processes involving bubbles and their impact on transport and reaction properties is crucial for optimizing PEM electrolyzers. Manual analyses of bubble distributions turn out to be inefficient, unreliable and expensive.

In this master science work, I have tackled the manual-analysis-related problem by making use of deep learning to develop reliable, less expensive and rapid approach to analyse bubble area distributions. The work encompassed the training and evaluation of a Unet (2D) model on a collection of 35 manually annotated images (at a scale of 25 mm) for semantic segmentation, followed by the analysis of bubble area distributions. The results obtained demonstrate good model performance and robustness.

Keywords: Artificial intelligence, deep learning, oxygen bubble dynamics, autonomous analysis, proton exchange membrane electrolyzers.

RÉSUMÉ

L'utilisation massive d'énergies fossiles due à une forte industrialisation et à une croissance démographique exponentielle est à la source du changement climatique d'origine humaine et de ses conséquences environnementales dévastatrices sans précédent, nécessitant une transition énergétique immédiate vers les technologies d'énergie renouvelable. Dans ce contexte, l'hydrogène vert, considéré à la fois comme un carburant et un moyen de stockage d'énergie, représente une option importante pour un changement énergétique efficace. Dans le but de produire et de stocker de l'hydrogène à grande échelle, d'importants efforts ont été déployés dans le domaine de la science des matériaux pour permettre le développement d'électrolyseurs à membrane échangeuse de protons (PEM) économiquement viables.

Cependant, les électrolyseurs d'eau souffrent d'une perte de performance en raison de la formation et de l'accumulation de bulles d'oxygène du côté anodique. Comprendre les processus impliquant ces bulles et leur impact sur les propriétés de transport et de réaction est crucial pour optimiser les électrolyseurs PEM. Les analyses manuelles des distributions de bulles se révèlent inefficaces, peu fiables et coûteuses.

Dans ce travail de master, j'ai abordé ce problème en utilisant l'apprentissage profond pour développer une approche fiable, moins coûteuse et rapide pour analyser les distributions de surface des bulles. Le travail a englobé l'‘entraînement et l'évaluation d'un modèle UNet (2D) sur une collection de 35 images annotées manuellement (à une échelle de 25 mm) pour la segmentation sémantique, suivie de l'analyse des distributions de surface des bulles. Les résultats obtenus démontrent de bonnes performances et une robustesse du modèle.

Mots-clés : Intelligence artificielle, apprentissage profond, dynamique des bulles d'oxygène, analyse autonome, électrolyseurs à membrane échangeuse de protons.

TABLE OF CONTENT

ACRONYMS AND ABBREVIATIONS

AI	Artificial Intelligence
ANN	Artificial Neural Network
BPP	Bipolar Plate
CL	Catalyst Layer
CNN	Convolutional Neural Network
DL	Deep Learning
DNN	Deep Neural Network
FCN	Fully Convolutional Network
FN	False Negative
FP	False Positive
GDL	Gas Diffusion Layer
HER	Hydrogen Evolution Reaction
IEA	International Energy Agency
IoU	Intersection over Union
MEA	Membrane Electrode Assembly
ML	Machine Learning
MLP	Multi-Layer Perceptron
MSE	Mean Squared Error
OER	Oxygen Evolution Reaction
PEM	Proton Exchange Membrane
PTL	Porous Transport Layer
R-CNN	Region-based Convolutional Neural Network
ReLU	Rectified Linear Unit
ROI	Region Of Interest
SEM	Scanning Electron Microscopy
SGD	Stochastic Gradient Descent
SPE	Solid Polymer Electrolyte
TEM	Transmission Electron Microscopy
TN	True Negative
TP	True Positive

LIST OF TABLES

LIST OF FIGURES

GENERAL INTRODUCTION

GENERAL INTRODUCTION

The widespread use of fossil fuels such as coal, natural gas, and oil, coupled with the ever-increasing world population since the industrial revolution, has led to climate change, depletion of fossil fuel reserves, health problems, and an increase in fossil fuel prices. The emission of greenhouse gases, particularly carbon dioxide, has several detrimental effects on human health, wildlife, trees, the environment, and the economy [1–2]. It is undeniable that the transportation sector is one of the primary industries responsible for a substantial rise in carbon emissions. This sector contributes approximately 13.5% to global warming [3], making it a major source of pollution. The transition to cleaner energy conversion and storage technologies is crucial in addressing the global challenges related to climate, health and economy.

In recent decades, significant progress has been made in the development of solar and wind technologies for renewable energy production. Solar panels and wind turbines are primarily integrated into the power sector to promote green initiatives [4]. However, it should be noted that both solar and wind technologies suffer from intermittency issues (solar panels do not generate electricity at night or on cloudy days, and wind turbines do not produce electricity during periods of no wind), which limit their reliability. A study conducted by Sarker et al. [5] suggests that hydrogen-based storage energy provides a viable solution to overcome the inconsistency associated with solar and wind energy. To achieve success in this endeavor, the successful deployment of proton exchange membrane (PEM) water electrolyzers is crucial. These electrolyzers offer rapid dynamic response and high energy efficiency enabling hydrogen production through water electrolysis [6].

Recent research suggests that the efficiency of PEM water electrolysis, a sustainable process for converting electricity into hydrogen and oxygen, is adversely affected by the accumulation of oxygen bubbles on the anode electrocatalyst layer [7–8]. Understanding the behavior of oxygen bubbles is thus crucial for optimizing the performance of PEM water electrolyzers [8]. However, the current method of analyzing bubble images manually is time-consuming, unreliable, and expensive [9]. Continuous efforts are underway in the field of research and development to automate the image analysis.

The primary goal of this thesis is to perform a deep learning-based analysis of images containing oxygen bubbles. The work encompasses two key aspects: training a UNet (2D) model to conduct semantic segmentation of bubbles in the provided images and extracting bubble areas for further distribution analysis.

This master’s thesis is divided into three main chapters. Chapter 1 provides a comprehensive review of existing literature. Chapter 2 describes the materials and methods employed in this study. Lastly, chapter 3 focuses on presenting the results obtained and discussing their implication.

CHAPTER 1:
LITERATURE REVIEW

CHAPTER 1: LITERATURE REVIEW

In this chapter, we conduct a review on the existing literature pertaining to the historical development of PEM electrolyzers, their operational principles and the dynamics of the oxygen bubbles formed, their current status in the field, and the ongoing challenges they face. Additionally, we provide a comprehensive review of the conventional bubble analysis approach and the emerging deep learning-based methods.

1. PROTON EXCHANGE MEMBRANE ELECTROLYZERS

1.1. HISTORY

PEM electrolyzers, also known as Proton Exchange Membrane electrolyzers or Polymer Electrolyte Membrane electrolyzers, are a type of electrolysis technology used to produce hydrogen gas through water splitting. The development of PEM electrolyzers can be attributed to advancements in fuel cell technology and the growing demand for efficient and eco-friendly methods of hydrogen production. The history of electrolyzers dates back to the discovery of electrolysis phenomenon in 1789 by Troostwijk and Diemann. This led to the development and refinement of alkaline electrolyzers [10]. However, alkaline electrolyzers faced limitations such as limited operational range at low loads, constrained current density, and low operating pressure [10].

In 1967, General Electric initiated the development of solid polymer electrolyte (SPE) electrolysis cells (Fig. 1.1). At that time, the maximum achievable current density was around 150 amps/ft2, with a voltage exceeding 2.0 V [11]. General Electric’s pioneering work in utilizing a solid polymer electrolyte (now known as polymer electrolyte membrane), represented a significant advancement in addressing the drawbacks associated with alkaline electrolyzers.

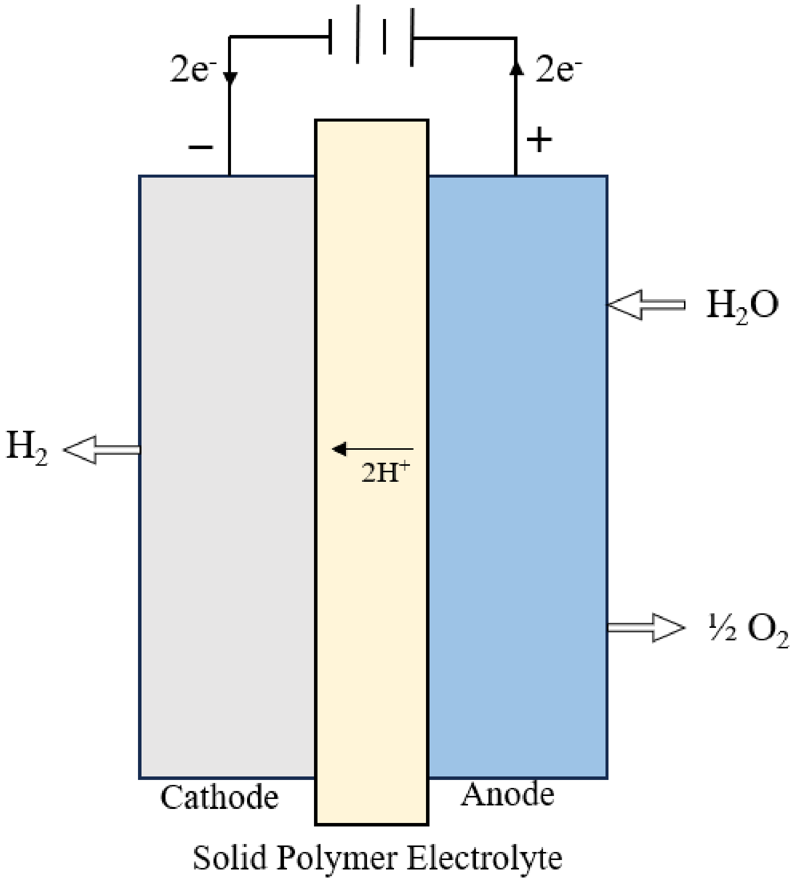

Fig. 1.1. SPE electrolysis cell schematic.

In 1973, Russell *et al.*[10] conducted pioneering research on PEM electrolysis as part of their work at General Electric. Figure 1.2 shows voltage-current curves obtained from 1967 to 1972 [10]. In the early stages of PEM water electrolysis development (1967), higher cell voltages (1.8 to 2 V) were needed to achieve current densities ranging from 0.125 to 0.150 Acm^{-2}. However, as advancements were made in catalysts, membranes, and electrodes during subsequent years, the same current densities were achieved at lower cell voltages (1.45 to 1.55 V in 1972), improving the performance of the PEM electrolyzers.

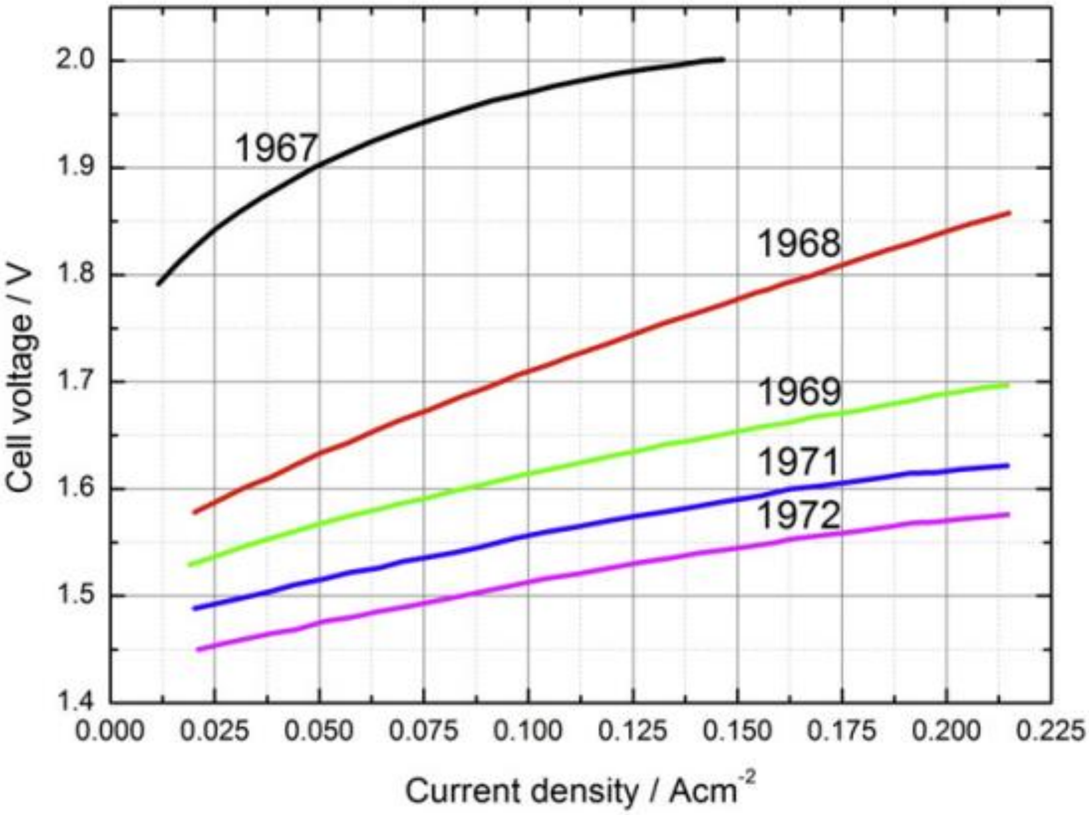

Fig. 1.2. Performances of PEM water electrolysis from 1967 to 1972. Cell at 48.8 degree Celsius and standard pressure [10].

Significant progress has been made in the development of PEM electrolyzers in recent years. In 2002, Onda and collaborators documented the first modeling of PEM electrolysis. They developed a two-dimensional simulation program to analyse PEM water electrolysis cells, incorporating conservation equations of mass, charge, and energy in both the water flow direction and perpendicular to the polymer film [12].

As of 2022, Lin *et al.*[13] conducted an investigation into the performance of PEM electrolyzers with various flow field configurations. The best output performance was observed in a PEM electrolyzer utilizing a parallel flow field with a channel width of 1 mm. Operating at 60 °C and 0.1 bar anode pressure, this configuration achieved at a current density of 1 A/cm^2 a potential of 2.1 V [13].

Currently, PEM water electrolyzers find applications in various fields, including hydrogen generation for electricity storage, stationary power, and chemical production such as ammonia and methanol. According to the International Energy Agency (IEA), the total installed capacity of PEM electrolyzers for the year 2023 is estimated to be 1,125 MW [14].

1.2. Working Principle

To gain a better understanding of the challenges associated with PEM electrolyzers, it is essential to familiarize oneself with the underlying working principle of this technology. A PEM water electrolyzer is an electrochemical device that utilizes an electrical current to split water molecules into hydrogen and oxygen molecules. Fig. 1.1 provides a schematic illustration of a PEM water electrolysis cell.

The electrolysis process in PEM electrolyzers is governed by two main reactions: the oxygen evolution reaction (OER), or water oxidation at the anode, and the hydrogen evolution reaction (HER) at the cathode. At the anode, water molecules decompose, resulting in the production of oxygen, protons, and electrons. The protons then migrate through the membrane and undergo reduction at the cathode, where they recombine with electrons to form hydrogen [15]. The formation of oxygen and hydrogen can be described by the following chemical equations,

$$H_2O\,(l) \longrightarrow \tfrac{1}{2}\,O_2\,(g) + 2H^+ + 2e^- \quad \text{(anode)} \qquad (1)$$

$$2H^+ + 2e^- \longrightarrow H_2\,(g) \quad \text{(cathode)} \qquad (2)$$

$$H_2O\,(l) \longrightarrow H_2\,(g) + \tfrac{1}{2}\,O_2\,(g) \quad \text{(overall)} \qquad (3)$$

During operation of a PEM electrolyzer, the electrochemical process is irreversible, leading to electrode polarization and a deviation of the potential from equilibrium. This deviation, referred to as overpotential (η), added to the cell voltage, which is the sum of the thermoneutral (or equilibrium) voltage (V_{th}) and η. The overpotential (η) is composed of several contributions, including activation overpotential (η_{act}), ohmic overpotential (η_{Ω}), and mass transport overpotential (η_m), as depicted in Fig. 1.3.

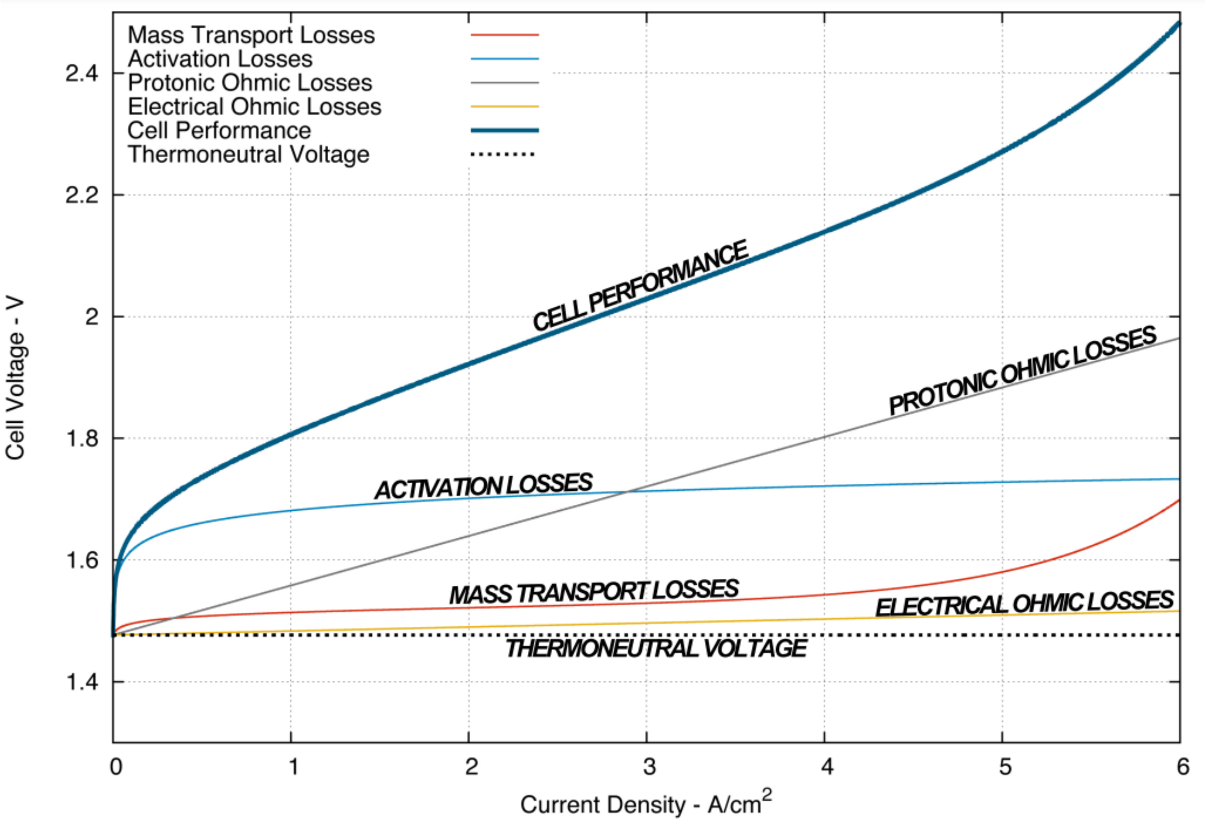

Fig. 1.3. Description of the various losses associated with the operation of a PEM electrolysis cell [16].

The processes underlying these contributions, collectively contribute to the complexity of the electrochemical device [15–17]. The η_{act} originates from contribution denoted as a specific step on a sequence of steps that control the overall reaction rate. η_{act} comprises two components: $\eta_{act,cath}$, which represents the activation at the cathode, and $\eta_{act,an}$, which represents the activation at the anode. On the other hand, η_{Ω} is due to the electrical resistance incurred by both electrons and ions, including the protonic resistance of the membrane. As the current density increases, η_{Ω} also increases, necessitating the minimization of the entire cell's resistance. Similarly, the η_m is closely linked to the current density as well. Furthermore, under high current density conditions, a large number of bubbles are generated in a short time span, which act as a shield over the active region and disrupt the contact between the electrode and electrolyte. As a consequence, the catalyst utilization rate decreases, resulting in an overpotential termed "bubble overpotential" ($\eta_{m,bub}$) [15].

A PEM water electrolysis cell consists of three essential components: the catalyst layer (CL), bipolar plate (BPP), and gas diffusion layer (GDL) [18], arranged in a sandwich configuration (Fig. 1.4).

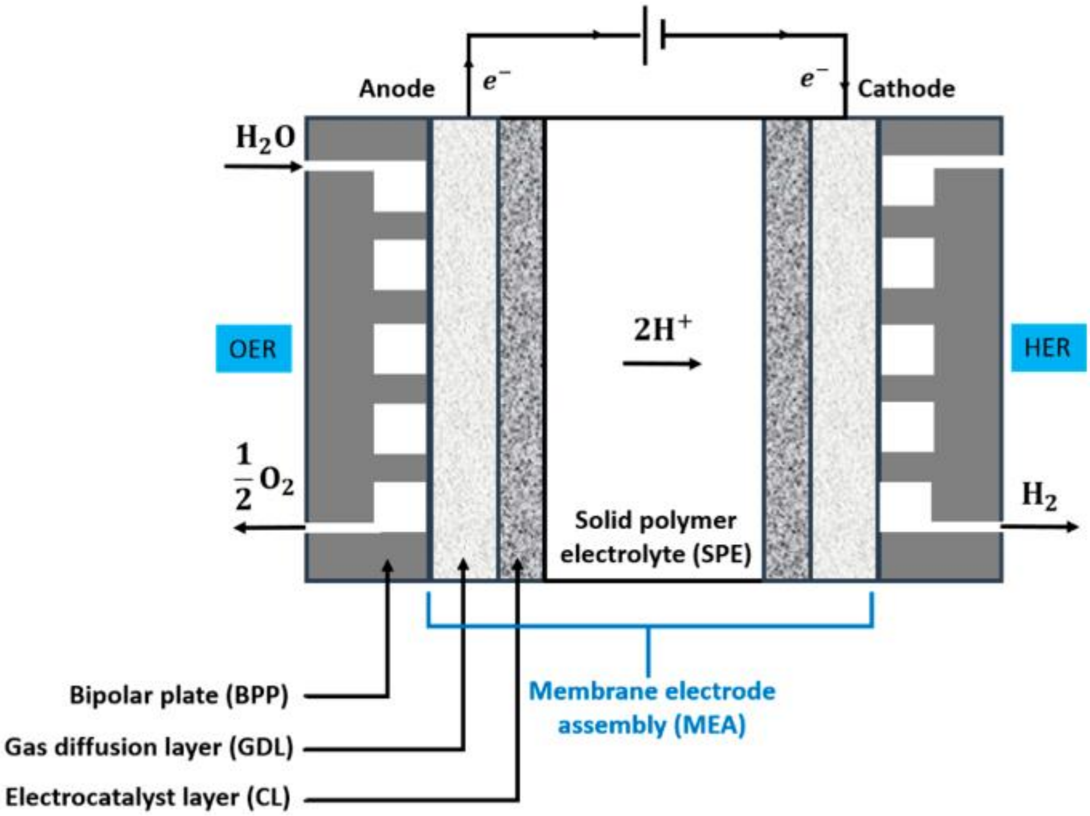
Anode
e^-
e^-
Cathode
H_2O
OER
$2H^+$
HER
$\frac{1}{2}O_2$
H_2
Solid polymer electrolyte (SPE)
Bipolar plate (BPP)
Gas diffusion layer (GDL)
Electrocatalyst layer (CL)
Membrane electrode assembly (MEA)

Fig. 1.4. Main components of a PEM water electrolyzer [19].

The bipolar plates and membrane electrode assembly enable the efficient conversion of electrical energy into hydrogen and oxygen gases within the PEM electrolysis cell. The followings provide additional details about these components.

Bipolar Plates (BPPs)

BPPs are an integral part of PEM water electrolyzer stacks, where multiple cells are connected in series. These plates serve several important functions, including facilitating mass transport, heat transfer, and electrical conductivity within the stack [20]. They provide structural support for the electrodes and membrane, ensuring uniform water distribution through flow fields. BPPs also conduct electrons between cells, establishing the electric circuit and connect adjacent cells in the stack. They also contribute to thermal conduction for effective temperature management. Moreover, the cost for BPPs significantly impacts the overall manufacturing cost of PEM water electrolyzers. The term "bipolar plate" derives from its contact with the anode side of one cell and the cathode side of the adjacent cell [21]. Fig. 1.5 illustrates the positioning of the BPP within the PEM water electrolyzer stack.

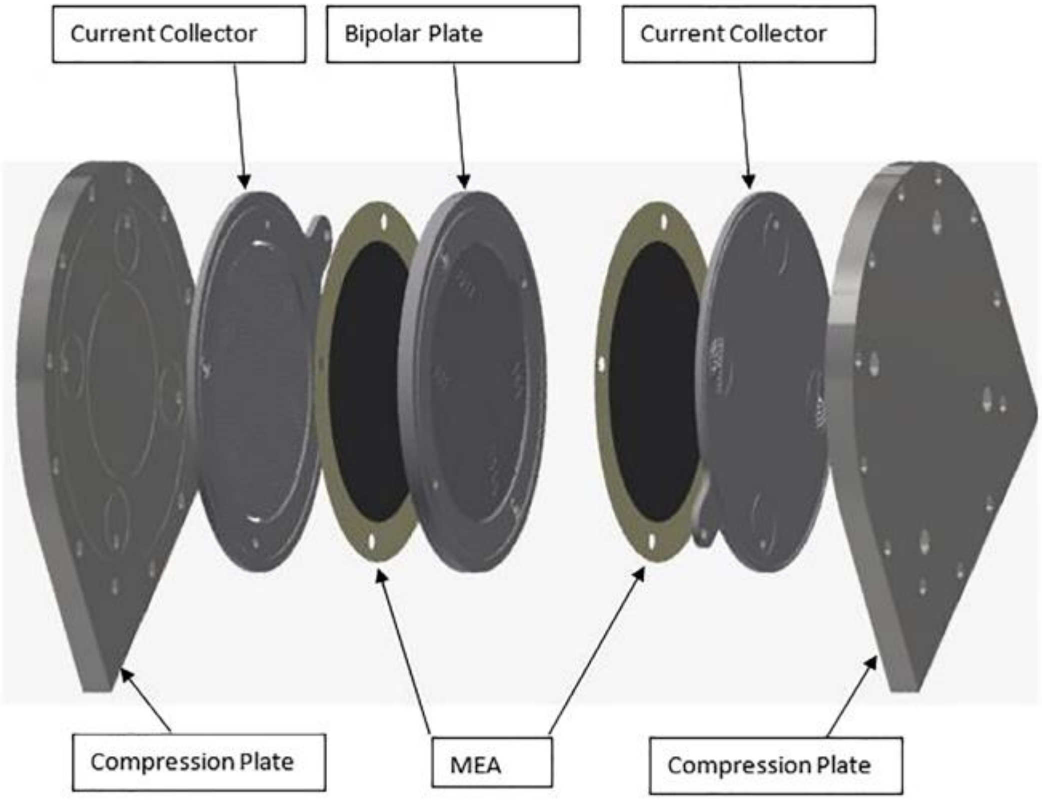

Fig. 1.5. Stack structure of PEM water electrolyzer [21].

Membrane Electrode Assembly (MEA)

The advancement of PEM water electrolysis technology relies on the continuous evolution of the device-level electrolyzer, which is heavily influenced by improvements in the smallest unit of the electrolysis cell called the membrane electrode assembly (MEA) [22]. The MEA is designed as a zero-gap cell, providing low ohmic resistance and efficient mass transport, resulting in higher energy efficiency at a reduced cost. However, for widespread commercialization, further enhancements are required in terms of MEA performance, cost, and durability [23–24]. As depicted in fig. 1.4, the MEA consists of three components: the gas diffusion layer (GDL), electrocatalyst layer (CL), and solid polymer electrolyte (SPE):

The gas diffusion layer (GDL) serves as a vital component, positioned between the catalyst and flow field. Its main functions are to conduct heat and electrons, and facilitate the movement of reactants (liquid water) and products (oxygen and hydrogen) while minimizing activation, thermal, ohmic, interfacial, and fluidic losses. To achieve this, the GDL must offer Simultaneous gas and liquid permeability, enabling reactants access the reaction sites from flow fields, and products from reaction sites move into flow channels, which reduce their local concentration to improve the performance. It should also exhibit effective electrical and thermal conductivity, facilitating electron flow away from the anodic reaction sites while providing a steady electron supply to cathodic reaction sites, ensuring optimal heat distribution. Additionally, the GDL requires robust interfacial and mechanical properties, including corrosion resistance and good contacts with the neighboring components like the bipolar plate and catalyst layer. All these requirements must be achieved without causing significant pressure drops in the flow channels [25].

The electrocatalyst layer (CL) serves as a site where multiple transport phenomena take place, including the transport of mass, electrons, and protons, all of these are essential for facilitating the electrochemical reactions. The CL is composed of a porous electrode structure that incorporates catalyst particles and an ionomer on the support material (Fig. 1.6). This ionomer not only functions as a binder to maintain the overall structure of the CL, but also forms a connected network for efficient proton transport. Additionally, the CL establishes stable interfaces between the solid catalyst particles and the liquid phase, creating active sites for electrocatalysis [26].

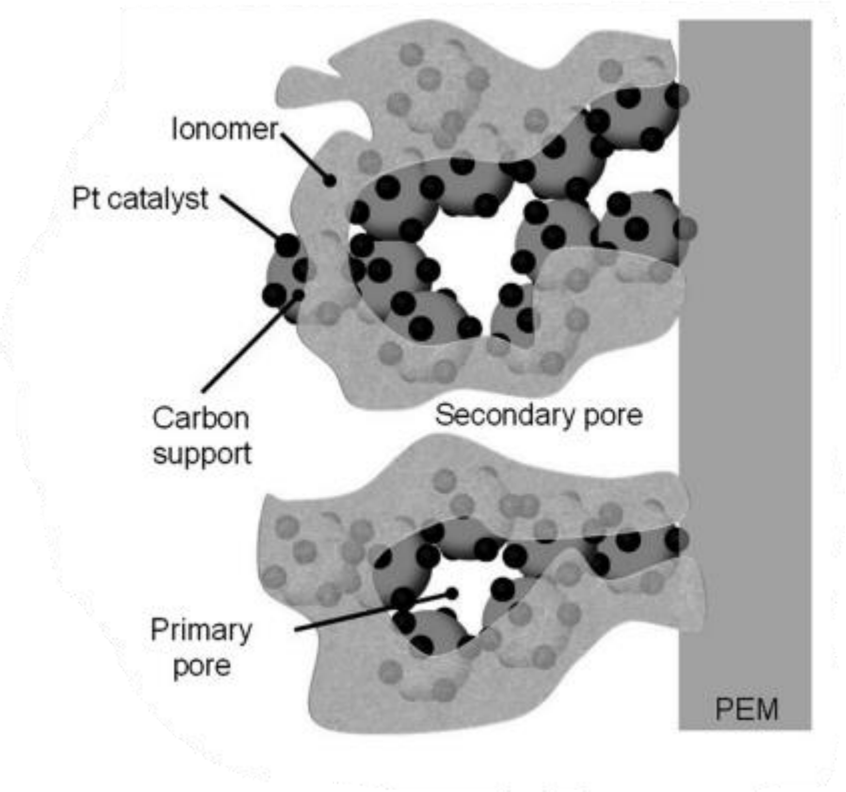

Fig. 1.6. A schematic illustration of a catalyst layer showing agglomerates of catalyst particles covered by Nafion ionomer, with primary pores inside the agglomerates and secondary pores between them [27].

The solid polymer electrolyte (SPE), also known as a polymer electrolyte membrane (PEM), is a polymeric film that facilitates the conduction of protons. It serves as an ionic conductive medium primarily in PEM water electrolyzers and PEM fuel cells. Perfluoro-sulfonated polymers, such as Nafion, are commonly utilized as the standard material for solid polymer electrolytes in conventional PEM systems, including the fuel cell technology [28]. Fig. 1.7 illustrates the chemical formula of Nafion.

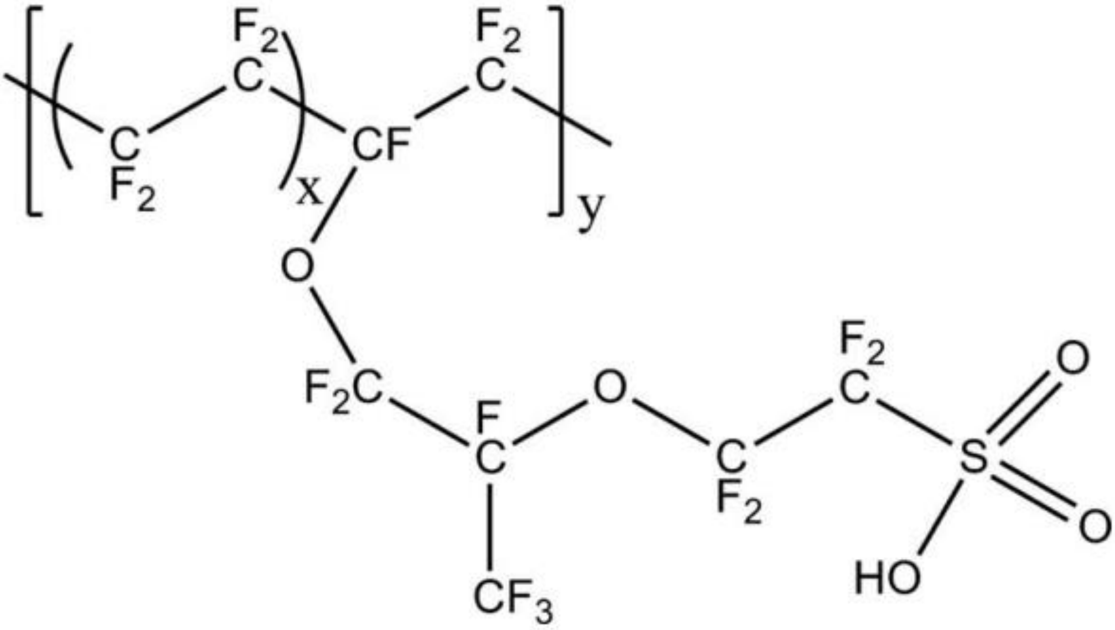

Fig. 1. 7. Chemical structure of Nafion molecule with x= 6 and y= 1 [29].

1.3. Oxygen Bubble Formation and Dynamics

Formation, growth and detachment of bubbles have received significant attention as researchers seek to unravel the complexities of two-phase flow phenomena occurring within PEM water electrolyzers. Inside a PEM water electrolyzer, oxygen bubbles form as a result of the oxygen evolution reaction (OER) taking place at the anode during the electrolysis process. Initially, the oxygen produced during OER dissolves in the water that covers the anode catalyst layer. However, due to substantial production of oxygen, the solubility limit of water is exceeded. This phenomenon, known as supersaturation, is responsible for the formation of oxygen bubbles [30].

Nouri-Khorasani *et al.* [31] illustrated the dynamic formation of oxygen bubbles within the transport layer (PTL) and flow channel (Fig. 1.8). In this illustration, oxygen bubbles originate at the anode catalyst layer, progress through the pores of the PTL, and combine with neighboring bubbles at the interface where the PTL meets the flow channel.

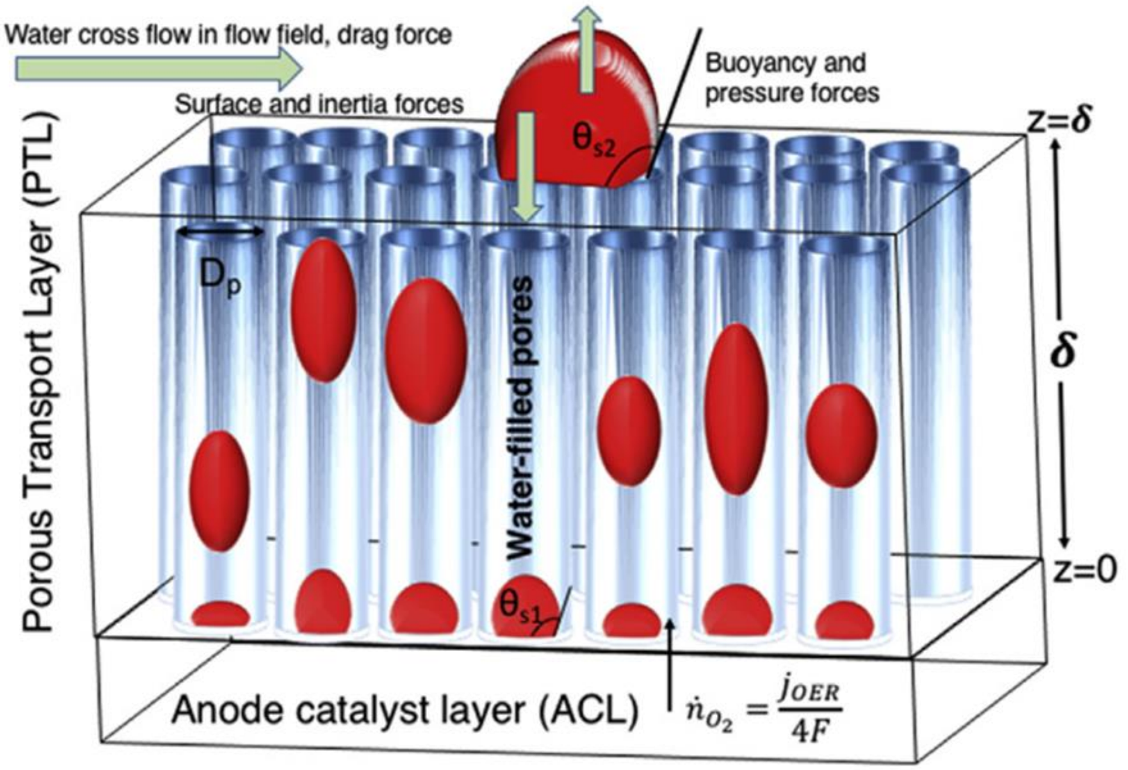
Water cross flow in flow field, drag force
Surface and inertia forces
Buoyancy and pressure forces
θ_{s2}
$z=\delta$
Porous Transport Layer (PTL)
D_p
Water-filled pores
δ
$z=0$
θ_{s1}
Anode catalyst layer (ACL)
$\dot{n}_{O_2} = \frac{j_{OER}}{4F}$

Fig. 1.8. Schematic of oxygen bubble growth in a PTL pore and flow channel [31].

The growth of oxygen bubbles within the pores of the PTL can be described in four sequential steps: 1. Oxygen bubble nucleation at the ACL-PTL interface. 2. The bubble undergoes spherical expansion within the pore of the PTL. 3. The bubble expands cylindrically along the PTL thickness. 4. Spherical expansion occurs through coalescence at the interface between the PTL and the flow channel [31]. The steps are illustrated in Fig. 1.9. At the cathode, the process of hydrogen bubble growth follows a similar mechanism to that observed for oxygen bubble growth on the anodic side.

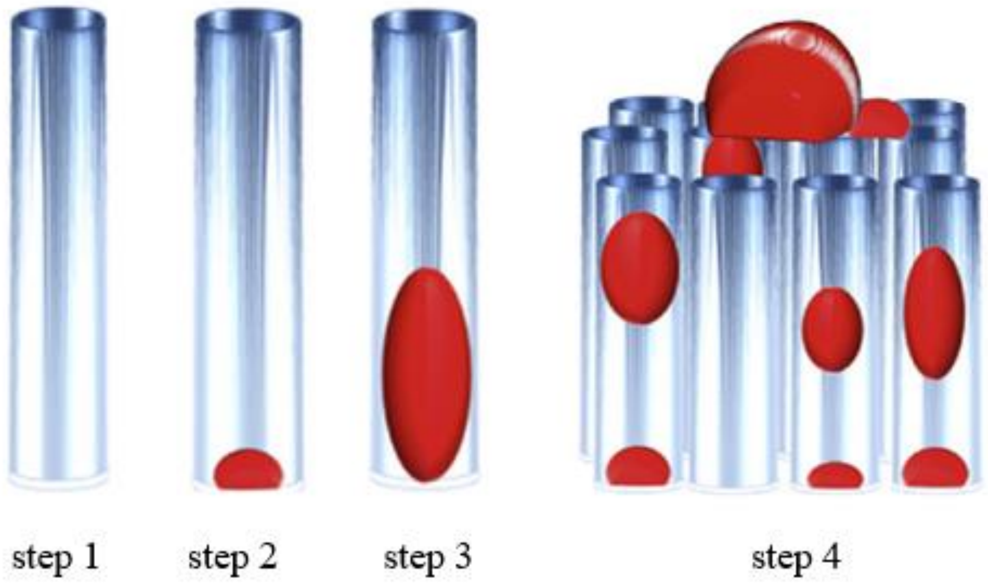

Fig. 1.9. Schematic presenting the different steps of oxygen bubble growth inside PTL pores [31].

As the bubble size gradually increases, the forces exerted by the flowing water and the resistance encountered from the incoming flow become more pronounced. This dominance of flow-induced force and drag force eventually leads to the detachment of bubbles from the electrocatalyst surface. The growth rate of bubbles is influenced by both the current density and flow velocity. Higher current density results in larger bubble detachment diameters, while increased flow velocity results in smaller bubble detachment diameters [32].

In contrast, the majority of hydrogen gas produced at cathode side can directly flow out the electrolysis cell without forming bubbles [7]. Hence, less emphasis is placed on the formation of hydrogen bubbles. Most of the bubbles are produced at the oxygen evolution reaction sites on the anode surface.

1.4. State-Of-The-Art and Current Challenges

In recent years, significant progress has been made in the development of PEM water electrolyzer technologies. These advancements have been characterized by the introduction of new cell components, configurations, and designs resulting in improved overall cell performance.

For instance, recently, Shi and colleagues developed a highly active and stable Ruthenium-based OER catalyst (SnRuOx) which enables a cell voltage of 1.565 V at 1 A cm^{-2} and exhibits long-term stability over 1300 hours with a degradation rate of 53 μVh^{-1} [33].

In addition, the exploration of new types of electrocatalysts (such as nanostructured electrocatalysts, metal-free electrocatalysts, metal sulfide-based electrocatalysts, transition metal oxide-based electrocatalysts, noble metal oxide-based electrocatalysts, etc.) has revealed remarkable capabilities in terms of electrocatalytic activity [34].

Despite tremendous efforts in advancing PEM water electrolyzers for large-scale implementation, there remain two major challenges that need to be addressed. The primary challenge is related to enhancing the oxygen evolution reaction [35]. The enhancement of OER leads to a substantial increase in the production of oxygen bubbles per unit volume and time, which accumulate and cover the surface of the anode catalyst layer. This bubble coverage results in several adverse effects, including low catalyst utilization as well as limitations in mass transport [7–31–36–37]. The second challenge pertains to the high cost of components used in PEM water electrolyzers such as bipolar plates or platinum-based and iridium-oxide-based catalyst materials (currently at US$60,670 kg^{-1}). These expensive components contribute to the overall cost of the electrolyzer system [33–38–39]. Addressing these challenges is crucial for the further development and widespread commercialization of PEM water electrolyzer technology.

2. AUTOMATION OF IMAGE ANALYSIS

2.1. Conventional Bubble Analysis Approach

For many years, the analysis of bubbles has relied on established mathematical models and manual processing of a large number of images obtained from imaging modalities such as scanning electron microscopy (SEM), transmission electron microscopy (TEM), synchrotron radiography, X-ray tomography, and optical camera.

While mathematical models provide valuable insights into bubble properties such as number of bubbles, bubble size, bubble distribution, and shape, they have their limitations. Firstly, these models often rely on simplified assumptions and idealized conditions [40–41], which may not fully capture the complexities of bubble behavior observed in real-world situations. Secondly, mathematical modeling may struggle to accurately characterize merging bubbles, and may not adequately account for variations in bubble size and shape over time.

Performing manual analysis on extensive imaging data presents significant challenges. It is a laborious and time-consuming task that often requires considerable effort to classify each image accurately. Furthermore, manual identification introduces the possibility of human error, leading to misidentification of bubbles. Lastly, the lack of reproducibility and consistency among different human inspectors results in varying outcomes [42].

2.2. Deep Learning-Based Approach

The emergence of artificial intelligence (AI), particularly deep learning, has brought about significant disruption in various industries through the automation of complex and repetitive tasks. The field of materials science has embraced this transformative technology and made remarkable progress in utilizing deep learning models, notably in the detection and analysis of gas bubbles.

In a study conducted by Sun *et al.* [43], a specially designed multi-task deep learning network that combined U-Net and ResNet models were employed to perform instance segmentation and extract fission gas bubbles on U-10Zr annular fuel. The proposed method demonstrated a notable improvement, obtaining an accuracy of 70%.

The Faster R-CNN model has been employed to automate identification of helium bubbles in irradiated X-750 micrographs by adjusting its hyperparameters and image setup. The primary goal of the proposed model was to determine the location, radii, and cumulative volumes of the bubbles. Accuracy levels of 93% were attained when analyzing micrographs captured at high magnifications, and reasonably accurate quantification of sample images at lower magnification was also achieved [42].

Kim and Park [44] developed the Mask R-CNN to automatically detect and extract the actual shape of bubbles, making it applicable across different types of bubbly flows. The model showed excellent performance with an average precision (AP_{50}) reaching 98%.

More recently, Jacobs and collaborators [45] employed a comprehensive deep learning-based semantic segmentation approach, using the Mask R-CNN model, to identify and quantify nanoscale cavities in irradiated alloys. Through rigorous evaluation using random leave-out cross-validation, the model provided precise assessments of material swelling, demonstrating an average mean absolute error of 0.30% swelling.

PARTIAL CONCLUSION

The introduction of PEM electrolyzer technology in 1967 by General Electric aimed to address the limitations of alkaline electrolyzers: limited operational range at low loads, constrained current density, and low operating pressure. The PEM electrolysis cell is made of key components such as SPE (Solid Polymer Electrolyte), CLs (Catalyst Layers), GDLs (Gas Diffusion Layers), and BPPs (Bipolar Plates). Its working principal is based on two main types of reactions: the hydrogen evolution reaction (HER) at the cathode, which generates hydrogen gas, and the oxygen evolution reaction (OER) at the anode, producing oxygen gas. The OER poses a challenge as the formation and accumulation of oxygen bubbles on the anode catalyst layer (CL) surface reduces the active reaction area between the reactant (water) and the CL leading to an increase in overpotential, and thereby reducing the overall efficiency of the PEM electrolyzer. Conventional and deep learning-based approaches are utilized to study the evolution of bubbles. However, the deep learning-based methods have shown to be more efficient in terms of reliability, time, and model execution speed.

CHAPTER 2: METHODS AND MATERIALS

CHAPTER 2: METHODS AND MATERIALS

This chaper gives a general understanding of deep learning, UNet model, as well as the explanation of the evaluation metrics and the data acquisition. Moreover, it places particular focus on detailing the methodological pipeline followed in this study.

1. FUNDAMENTALS OF DEEP LEARNING

1.1. Overview of Artificial Intelligence, Machine Learning and Deep Learning

In order to gain a comprehensive grasp of Deep Learning (DL), it is essential to begin with an exploration of the concepts of Artificial Intelligence (AI) and Machine Learning (ML). DL, as a subfield of ML, inherently lies within the broader domain of AI, as depicted in Fig 2.1.

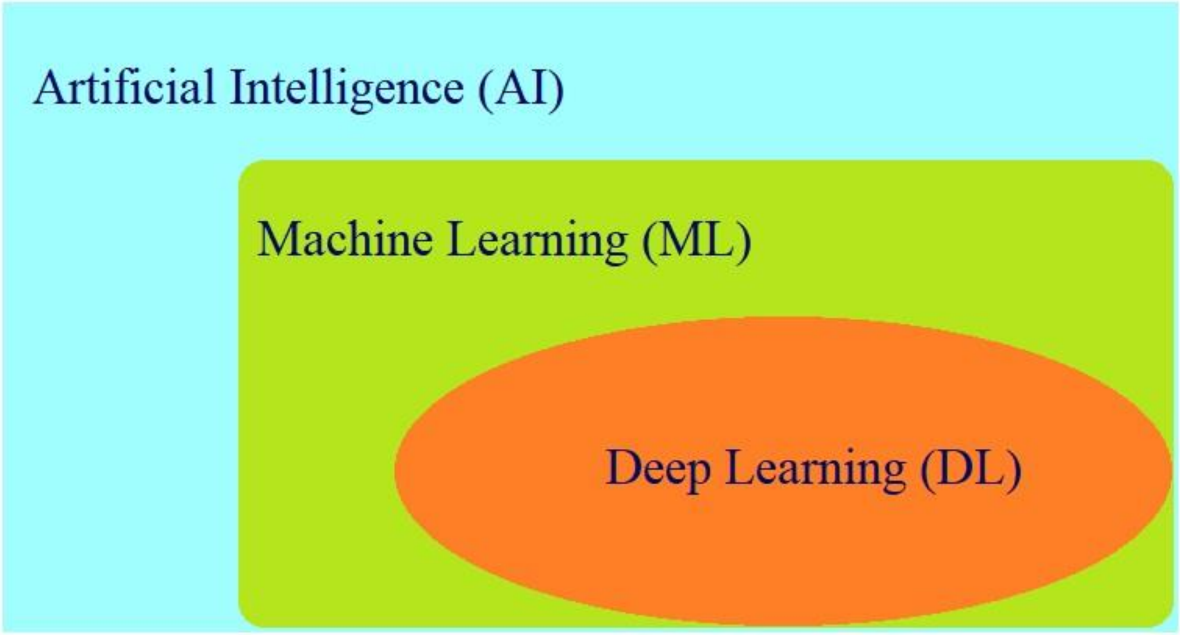

Fig. 2.1. Schematic representing the branches of artificial intelligence.

Artificial Intelligence (AI)

AI is a discipline in Computer Science that revolves around the automation of intelligent behavior [46]. It entails employing computational techniques to mimic human cognitive activities, encompassing tasks such as interpretation, inference, decision-making, estimation, classification, and possessing the capacity to understand languages, learn, reason, and resolve problems [47–48]. The primary aim of AI research is to enhance the ability of computers to rapidly and effectively execute cognitive tasks, mirroring human capabilities with high accuracy and efficiency. AI-based problem-solving approaches can be categorized as strong AI, which seeks to imitate human mental processes for thinking and reasoning, and weak AI, which involves specific task-oriented computational software without involving human-like intuitive processes [47].

Machine Learning (ML)

ML is a subset of AI that comprises algorithms, which learn from datasets provided to make predictions and inferences without the need for explicit programming. A subset of machine learning algorithms relies on statistical learning techniques to comprehend and interpret data. These statistical methods are particularly effective for solving problems with linear relationships between input data and output, like in the cases of linear and logistic regression. The concept of machine learning involves three main learning categories: supervised, unsupervised, and reinforcement learning [47], as illustrated in Fig. 2.2.

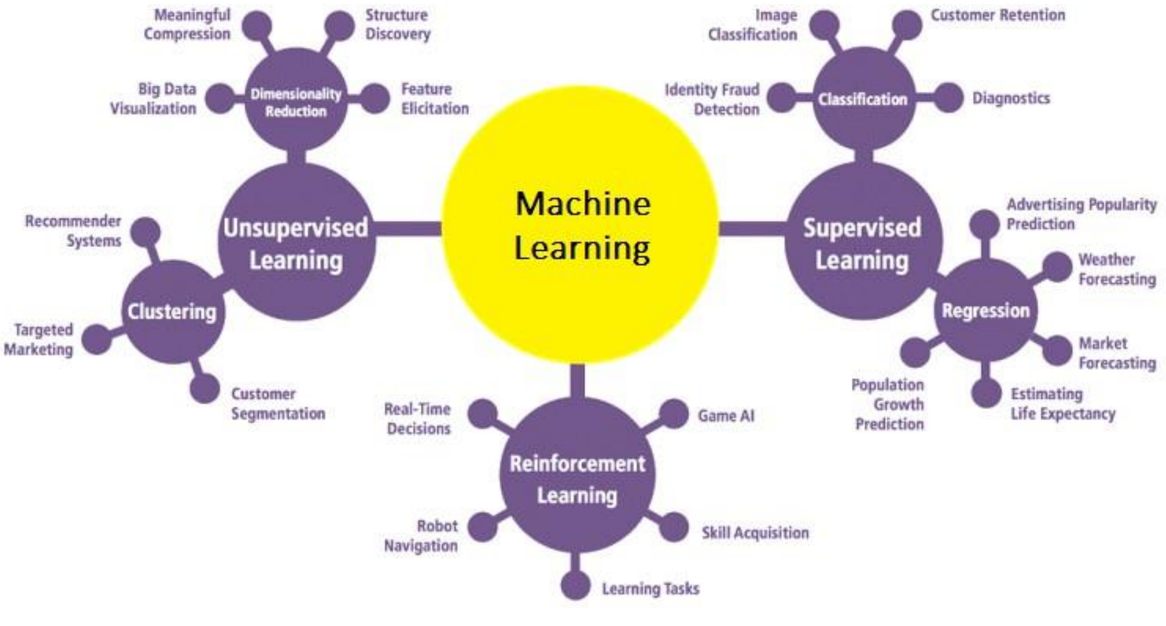

Fig. 2.2. Illustration ML's learning categories [47].

In supervised learning, every set of data used for model training is associated with a corresponding label. Through this process, the model learns to establish a relationship between input data and its corresponding output, allowing for the creation of a mapping between the two. Unsupervised learning, in contrast, involves working with unlabeled training data, making it difficult to assess the model's accuracy. In this type of learning, the model learns by extracting features from the training data in order to classify them in different categories. Lastly, reinforcement learning is a ML training approach where an agent (learning system) learns through a process of receiving rewards for exhibiting desirable actions and penalties for undesirable ones. In reinforcement learning tasks, the agent interacts with an environment, observing its current state, and takes actions to optimize its cumulative long-term rewards, which are represented by numerical signals [49–50].

Deep Learning (DL)

DL is a branch of machine learning (ML) that uses algorithms, the designs of which are based on the structure and function of the brain's neural networks. Consequently, deep learning networks are usually referred to as artificial neural networks (ANNs), which will be further discussed in the following section. Like ML, DL utilizes algorithms to analyze data, learn from them, and subsequently make predictions or determinations about new data. Numerous research studies have demonstrated that deep learning is essential for solving artificial intelligence tasks such as target recognition, speech perception, and language understanding, as it enables the learning of complex functions that capture high-order abstract concepts [51].

Artificial neural networks (ANNs) are nested functions made of units called perceptrons or neurons which are interconnected [52]. The neurons are organized in input layer, hidden layer(s), and output layer as illustrated in Fig. 2.3.

1.2. Basics of Artificial Neural Networks

Artificial neural networks (ANNs) are essentially nested functions made of units called perceptrons or neurons [52]. In a graph representation of ANNs, the neurons are organized in input layer, hidden layer(s), and output layer as illustrated in Fig. 2.3.

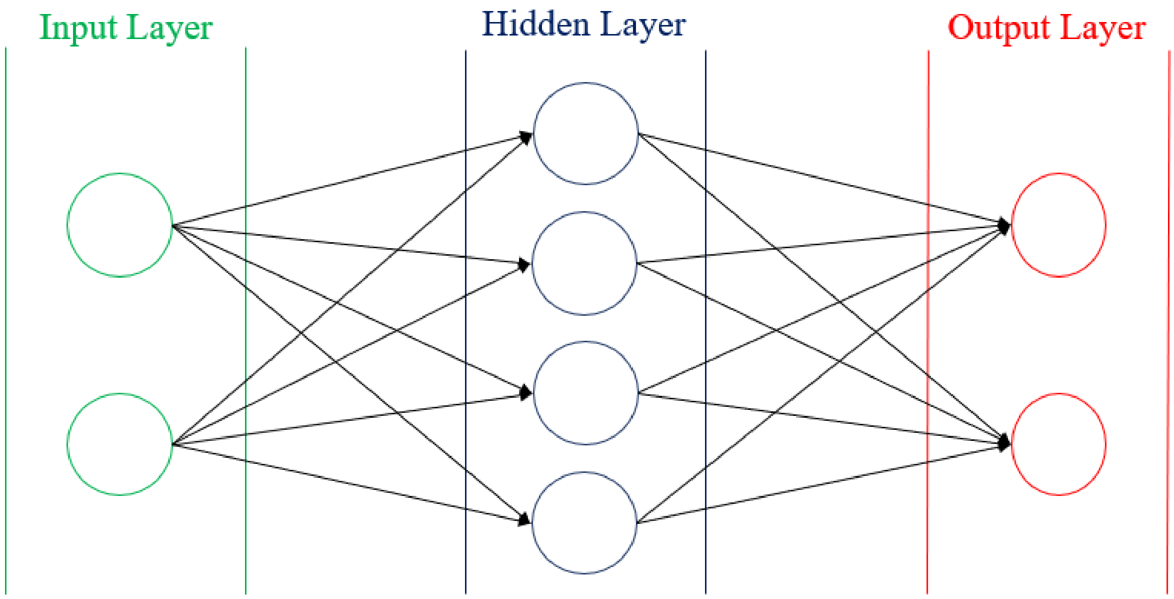

Fig. 2.3. Schematic of an ANN showing the organization of the perceptrons.

The input layer is the first layer of the neural network, responsible for receiving the input data and forwarding it through the network for further processing. A hidden layer, on the other hand, acts as an intermediary layer between the input and output layers. Its main function is to capture patterns from the input data to facilitate learning. Lastly, the output layer serves as the final layer of the neural network, generating predictions based on the knowledge acquired from the input data and processed through the hidden layer (s). We refer to a deep neural network (DNN) when the number of hidden layers within an ANN is greater than 1. This concept also explains the adjective "deep" in deep learning (DL).

In an ANN, a receiving perceptron processes the signal, and signals the downstream perceptrons connected to it. The processing involved within the perceptron's structure is depicted in Fig. 2.4. The perceptron's output, denoted as y, is determined by its activation function, which takes as input the weighted sum of the input signals (x_1, x_2, ..., x_N) along with an additional bias term (denoted b). The activation function processes this input to produce the final output of the perceptron.

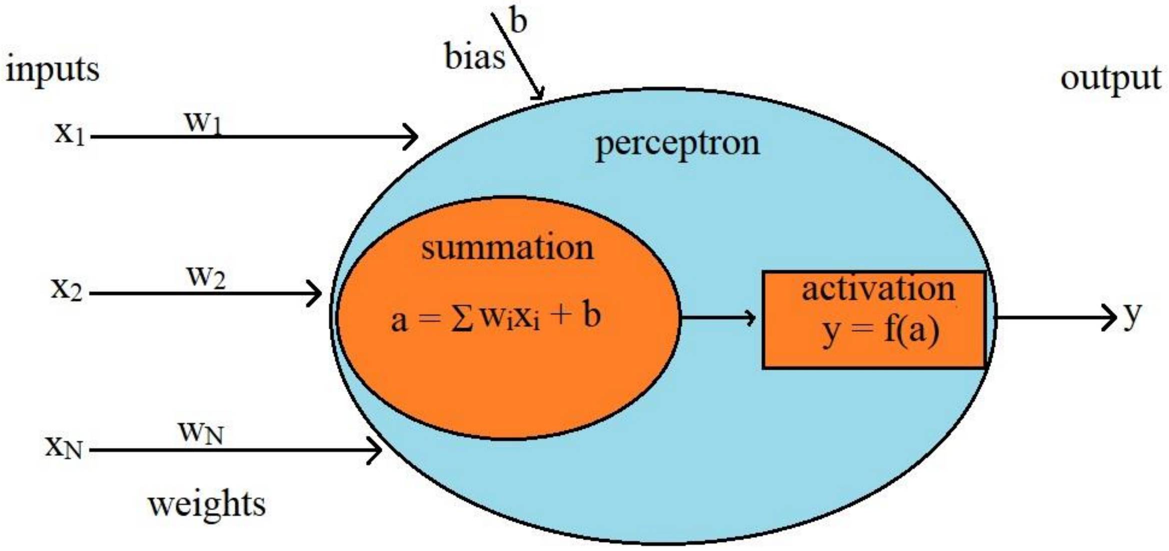

Fig. 2.4. Schematic of a perceptron describing a signal processing.

The learning within a neural network is commonly executed through the processing of input, which is also referred to as "training." This training process involves iteratively adjusting the connection weights and biases of the nested function [51]. In a specified order, an iteration comprises 3 steps: feedforward, loss computation, and back propagation. A neural network that includes a feedforward mechanism is commonly known as a multilayer perceptron (MLP) [53]. Fig. 2.5 illustrates a simple representation of a MLP and is used to explain these 3 steps.

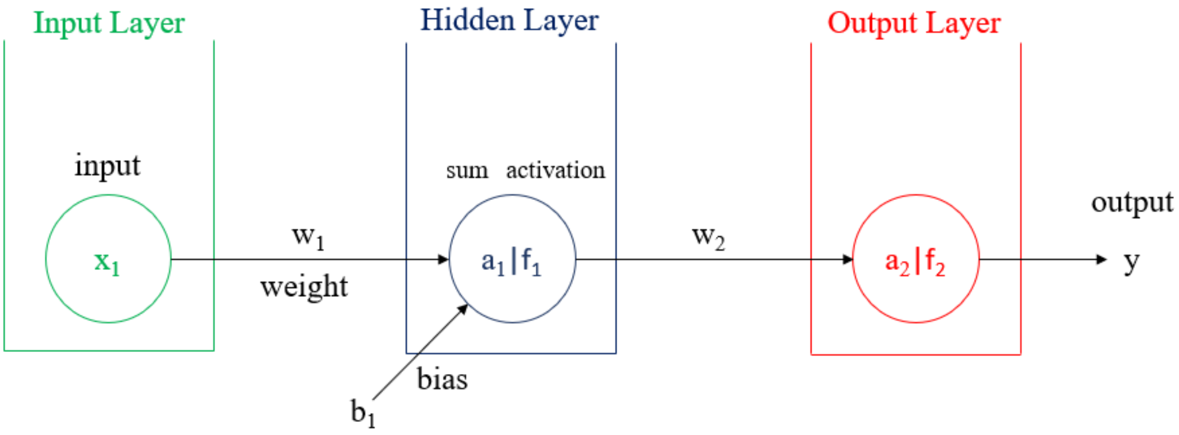

Fig. 2.5. Simplified representation scheme of a multi-layer perceptron.

The explanation is also based on a given set of samples x_i, its corresponding labels $\hat{y}_i$, and a standard multi-layer perceptron (MLP),

$$y = f_{MLP}(x; \theta), \tag{4}$$

with

$$\theta = \{f, w, b\}. \tag{5}$$

where y is output, f the activation function, w the weight, b the bias, and θ the model's parameters

Step 1) Feedforward

The original data is passed through the MLP, which has its weights initialized randomly. This forward pass is done by applying a series of nested equations (6) to each perceptron in the forward layers of the network.

$$a_1 = w_1 . x_1 + b_1 \tag{6a}$$

$$a_2 = w_2 . f_1(w_1 . x_1 + b_1) \tag{6b}$$

$$y = f_2(w_2 . f_1(w_1 . x_1 + b_1)) \tag{6c}$$

Here, a_i represents weighted sum of a perceptron's input signal (w_i . x_i) plus, the bias b_1.

The prediction process of a neural network on data can be understood through equations 6a-6c. In the hidden layer, the input x_1 is multiplied by a weight w_1, and the bias of the network, b_1, is added to the result. This value is then passed through a nonlinear activation function, f_1, and forwarded to the next layer which represents in our case the output layer. The same process is repeated for the perceptron in the output layer, where the final prediction, y, is obtained, representing the network's final output.

If the network was designed with multiple hidden layers, the initial process would be repeated for each neuron in subsequent layers, with the transformed value from each neuron being passed to the next layer until the final output is obtained.

Step 2) Loss calculation

After the forward propagation process, the predicted value, $y_{i,}$ is compared to the true value, $\hat{y}_i$, to determine the loss. This is done by calculating the difference between each individual true value, $\hat{y}_i$, and its corresponding prediction value, y_i. At the end of each iteration, the loss of each input is accumulated and passed through a loss function (L). The commonly used loss function is called Mean Squared Error (MSE). Equation (7) provides a mathematical representation of this function.

$$L = \frac{1}{N}\sum_{i=1}^{N}(y_i - \hat{y}_i)^2 \tag{7}$$

with L being the loss function, y_i the predicted value, $\hat{y}_i$ the true value, and N the total number of data points being used for training.

Step 3) Backpropagation

The objective of backpropagation is to optimize the learnable parameters, such as weights and biases, within a neural network by making adjustments to them. Once the loss is known, the optimization process typically involves using the stochastic gradient descent (SGD) optimizer [54]. SGD works towards minimizing the loss by calculating the derivative of the loss with respect to each weight in the network (as depicted in Fig. 2.6). This derivative is then utilized to update the weights. The weight update is performed by incorporating a learning rate, which determines the magnitude of the adjustment made to the weights. By iteratively updating the weights based on the loss derivative and learning rate, the network parameters are optimized to minimize the overall loss.

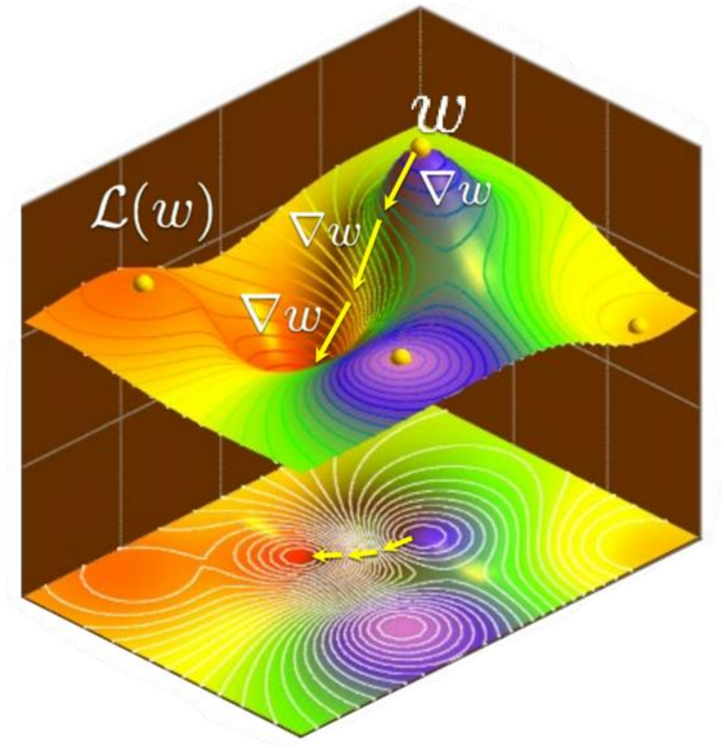

Fig. 2.6. descriptive scheme of SGD approach [55].

The whole process is called “backpropagation” because it updates the network's learnable parameters in a backward direction, from the output layer to the input layer (as illustrated in Fig. 2.7). This means that during the training process, the error or loss calculated at the output layer is propagated back through the network to adjust the weights and biases of the perceptrons in the hidden layer(s) and ultimately the input layer. By iteratively updating these parameters in the opposite direction of the data flow during the feedforward process, the network learns to minimize the error and improve its predictions over time.

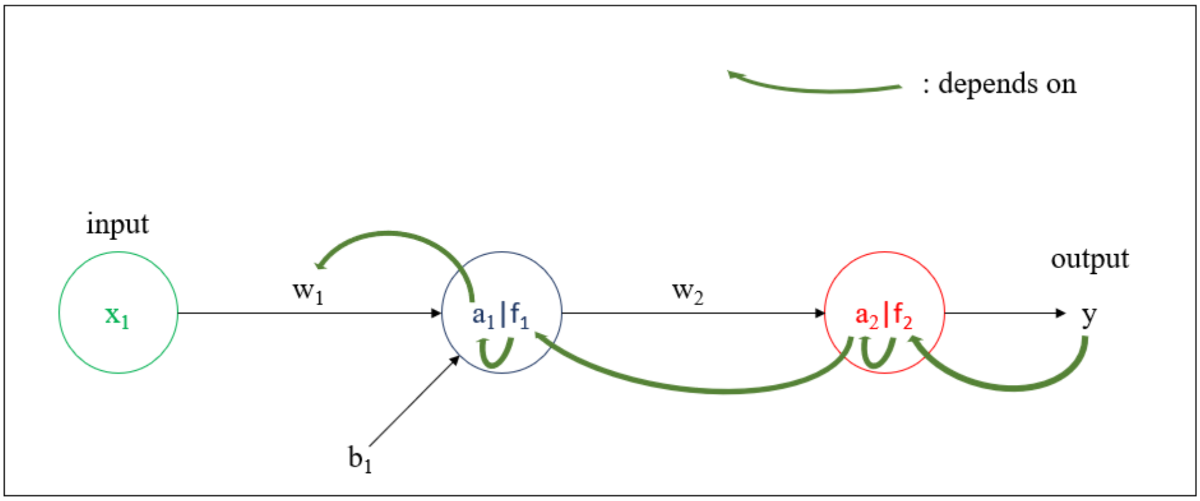

Fig. 2.7. Illustrative scheme of backward propagation showing the dependencies between the output, the activation functions, the weighted sums, and the weights.

By referring to fig. 2.7, it becomes evident that the output of each perceptron relies on the output generated by the perceptrons in the preceding layer. Hence, the determination of the loss gradient (∇w) for each weight (w_1 and w_2) in the MLP is done by initially computing the chained partial derivatives ∇w_2, and subsequently calculating ∇w_1 using the **chain rule**, as shown in equations (8):

$$\nabla_{w2} = \frac{\partial L}{\partial w_2} = \frac{\partial L}{\partial f_2}\frac{\partial f_2}{\partial a_2}\frac{\partial a_2}{\partial w_2} \tag{8a}$$

$$\nabla_{w1} = \frac{\partial L}{\partial w_1} = \frac{\partial L}{\partial f_2}\frac{\partial f_2}{\partial a_2}\frac{\partial a_2}{\partial f_1}\frac{\partial f_1}{\partial w_1} \tag{8b}$$

It is important to note that ∂w_2 equals ∂f_1. A simplification of ∇_{w1} gives,

$$\nabla_{w1} = \frac{\partial L}{\partial w_1} = \frac{\partial f_1}{\partial w_1} \times \nabla_{w2} \tag{8c}$$

The weight update is carried out by using the equation (9):

$$w_{new} = w_i - \eta \nabla w_i \tag{9}$$

where η is the learning rate, and w_{new} represents the updated weight.

1.3. Convolutional Neural Networks

Convolutional neural networks (CNNs), also known as ConvNets, are AI systems that employ deep learning to identify, recognize and classify objects, and perform detection and segmentation tasks for images and videos [56]. Furthermore, they are a class of artificial neural networks inspired by the concept that neurons in the visual cortex of the brain detect and identify features [57]. In a typical CNN for image classification, there are three main types of layers: convolutional layers that apply filters by convolving them across the input data; pooling layers that reduce the data dimensions by combining cluster outputs; and a single fully-connected layer that performs the final classification task [58]. A general architecture of a CNN is given in Fig. 2.8.

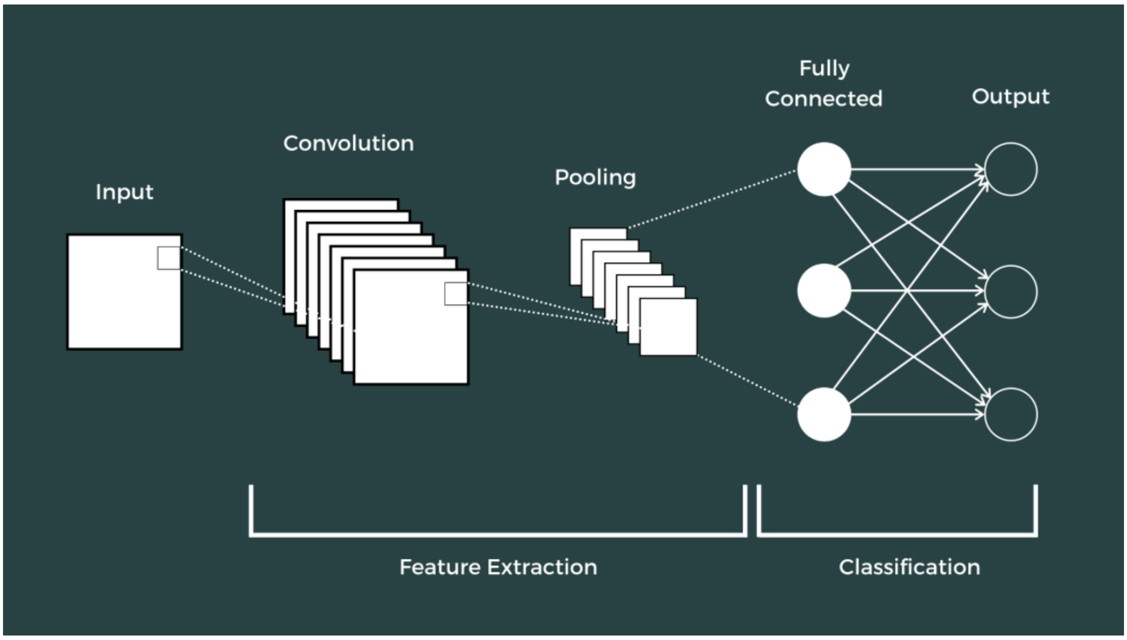

Fig. 2.8. Schematic of a convolutional neural network [58].

Convolution Operation

A convolutional layer consists of a collection of filters, or kernels (each kernel is a set discrete values or integers) that are applied to the input data. These kernels are characterized by their widths, heights, and weights, and they are used to extract features from the input data. The kernel weights start as random values but are gradually refined during training based on the data [56]. Convolution consists of performing a sliding motion of a filter, initially moving horizontally and then vertically over the entire image. An example using a filter of 2×2 pixels with a stride of 1 (step size of the horizontal and vertical slide) on an input image of dimension 4×4 pixels, is illustrated in Fig. 2.9

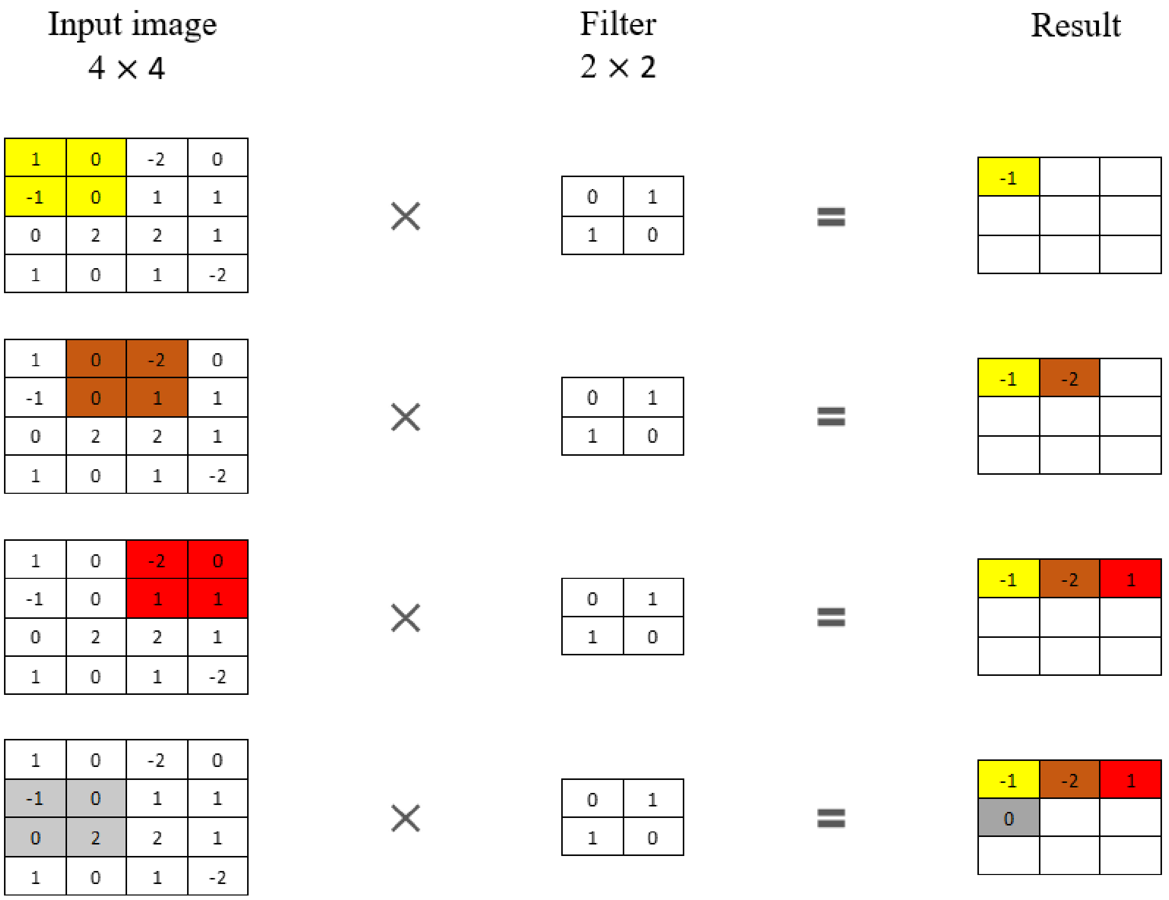

Fig. 2.9. Illustration of a convolution operation.

Pooling Operation

The pooling layer, referred to as the down-sampling layer, reduces the size of feature maps while preserving essential information contained within the input data [56]. The pooling operation consists of applying the filter by sliding it over the pooling layer, which results in obtaining either the maximum value from each window of the layer, the average value from each window of the layer, or the global average value from the entire layer, as depicted in Fig. 2.10.

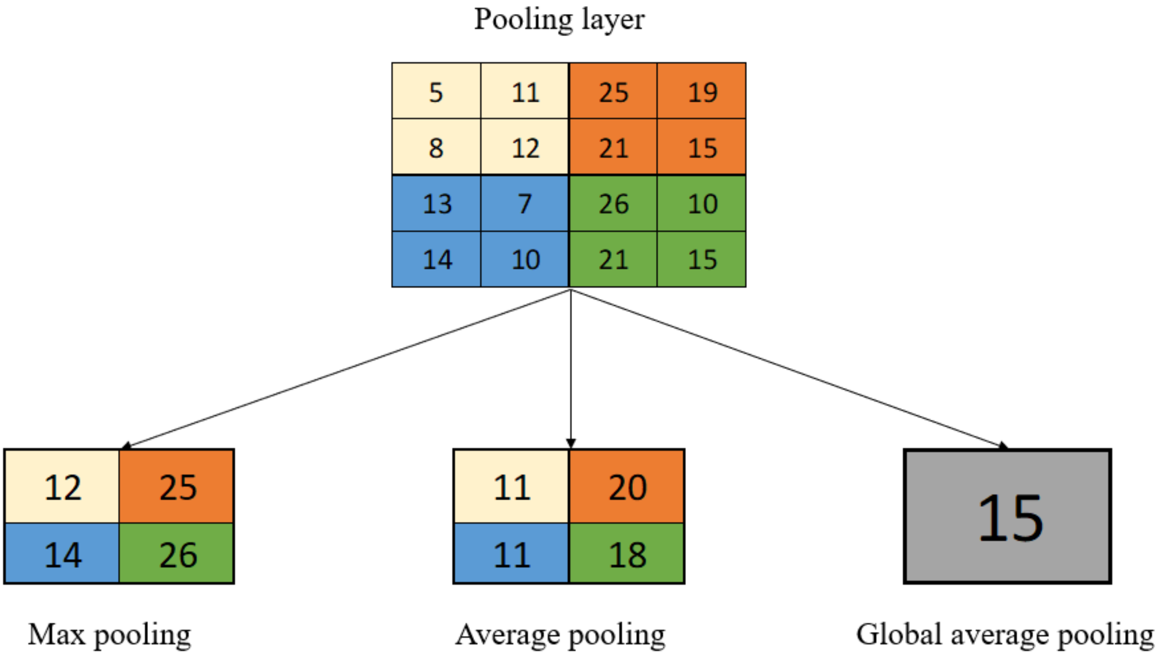

Fig. 2.10. Illustration of maximum, average, and global pooling operation.

The CNN architecture involves the convolution layer and pooling layer working in tandem (operate together in a coordinated and complementary manner). This arrangement serves to decrease computation time and enhance the network's ability to handle translation, scaling, and other types of deformations. The core concepts behind CNNs are the utilization of shared weights and local connections. By employing shared weights, the network avoids overfitting, while local connections reduce the number of parameters and simplify the computational complexity [59]. Two popular adaptations of the CNN architecture for image classification and object detection are the Fully Convolutional Network (FCN) and the Region-based Convolutional Neural Network (R-CNN). Fig. 2.11 illustrates the structure of FCN and R-CNN.

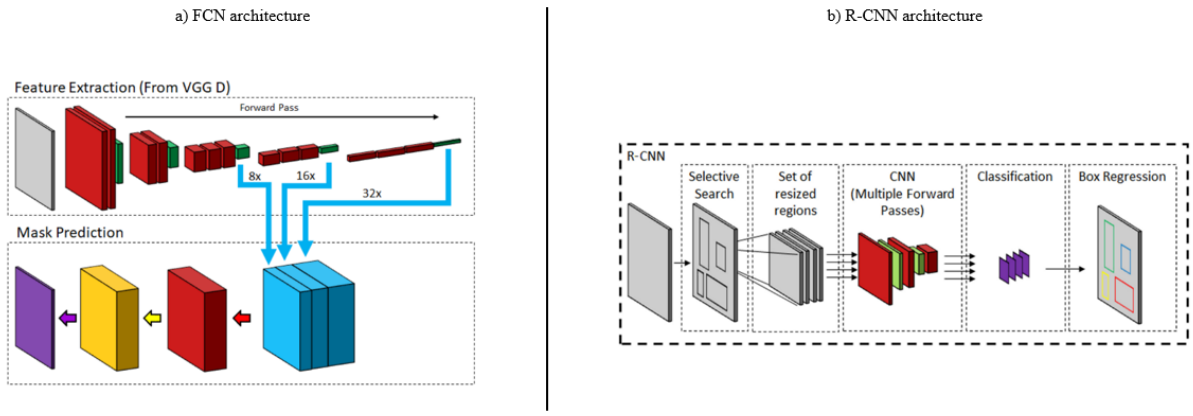

Fig. 2.11. Representations of FCN and R-CNN architectures with image segmentation with concatenated multi-scale features [60].

The Fully Convolutional Network (FCN) served as the foundational model from which the most successful, and advanced deep learning models for semantic segmentation have emerged [61]. A semantic image segmentation (as shown in Fig. 2.12) consists of assigning a corresponding class label to each pixel in an image. The desired output in semantic segmentation is a high-resolution image, typically of the same size as the input image, where each pixel is assigned to a specific class based on its representation [62].

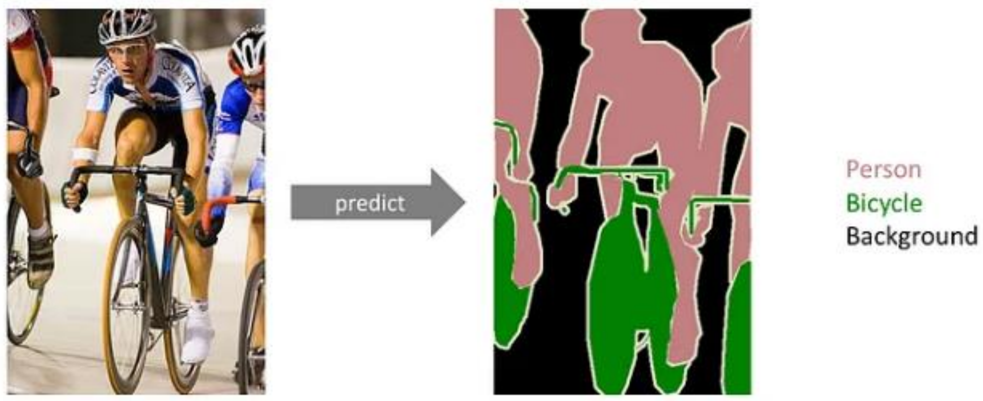

Fig. 2.12. Semantic image segmentation illustration [62].

UNet (2D) model is among these state-of-the-art deep learning models that have evolved from the FCN, and represents the considered model in our study.

2. UNET (2D) MODEL

The initial development of the UNet model took place in 2015 at the computer science department of the University of Freiburg in Germany, with the vision of analysing biomedical images. The original UNet architecture is depicted in Fig. 2.13. It is basically divided into two distinct sections: the **encoder** referred to as the contracting path on the left side, and the **decoder** known as the expansive path on the right side [63]. These sections are structured in a U shape, collectively forming the overall framework. The encoder section, consisting of five blocks, is responsible for downsampling the input feature maps to extract low-level features. Each block in the encoder contains two 3 × 3 convolutional layers with rectified linear unit (ReLU) activations, followed by a 2 × 2 max-pooling layer. The fifth block in the encoder does not include a pooling layer. On the other hand, the decoder section, also comprised of five blocks, functions as the inverse of the downsampling path. Each decoder block includes a 2 × 2 up-convolution (which performs upsampling of the features), followed by two 3 × 3 convolutions with ReLU activations. The fifth decoder block additionally incorporates a 1 × 1 convolution [64].

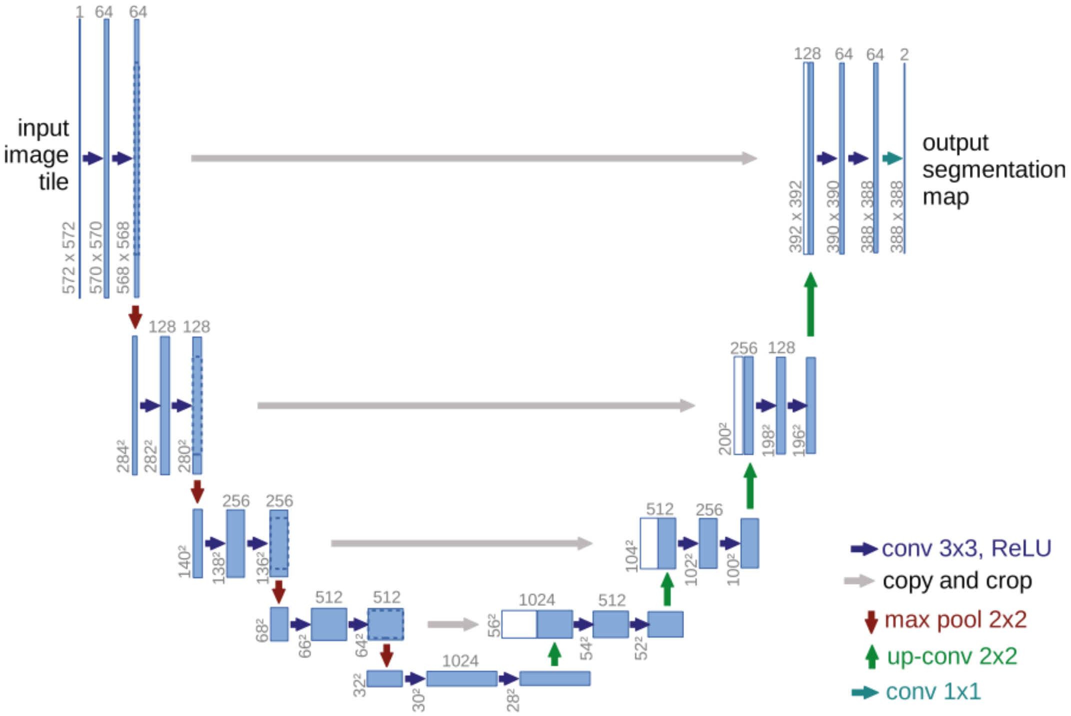

Fig. 2. 13. Original scheme of the UNet architecture [63].

3. EVALUATION METRICS

In the context of deep learning, an evaluation metric is a quantitative measure used to assess the performance, or quality of a model. The common evaluation metrics used in the literature are intersection over union (IoU), accuracy, precision, recall, and F1-score.

The classification of an object is primarily based on the intersection over union (IoU) measure along with a predefined threshold value. The IoU is determined by computing the ratio of the overlap area between two bounding boxes to the union area of these boxes, as depicted in Fig. 2.14. The IoU value ranges from 0 to 1. Therefore, the closer to 1, the better the performance. The model considers a prediction as correct when the IoU is greater than the defined threshold value. A good prediction is considered when the detection overpasses an IoU of 0.5.

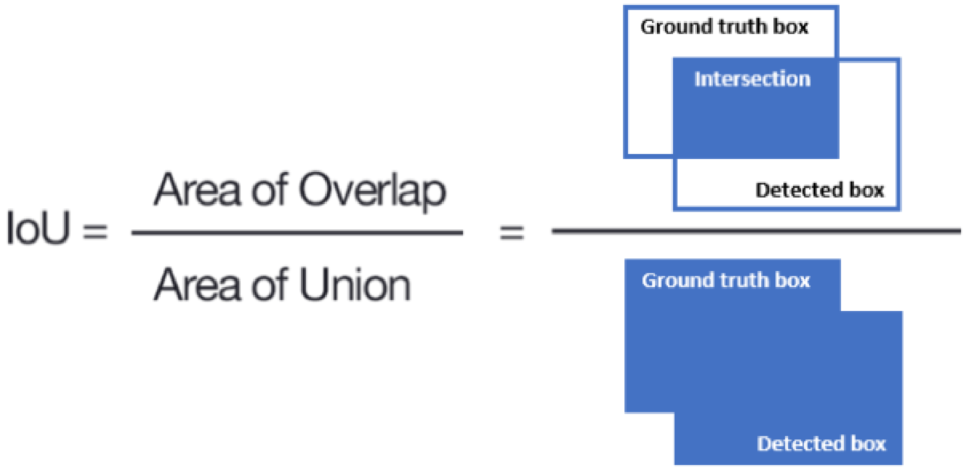

Fig. 2.14. Computing illustration of IoU metric [65].

Estimating performance involves making predictions about how well a model will perform or the loss it will experience when predicting on unseen data. This estimation is typically based on performance metrics derived from the confusion matrix [58]. In the context of a bubble detection problem, as depicted in table 2.1, the confusion matrix illustrates the predicted class (the classification made by the model) and the actual class (the true values of the data, known as ground-truth).

Table 2.1. Illustration of confusion matrix in the case of bubble identification.

		Actual Value		
		Bubbles	Non-bubbles	Total
Predicted Value	Bubbles	TP	FP	All predicted as bubbles
	Non-bubbles	FN	TN	All predicted as non-bubbles
	Total	All bubbles	All non-bubbles	All

For the purpose of this project, the explanation of the metrics is based on the specific addressed problem. The primary goal is to detect bubbles, so bubble is considered as positive class, while non-bubble referred to negative class. TP (True Positives) indicates the number of semantic entities accurately identified as bubbles. On the other hand, FP (False Positives) represents the number of semantic entities incorrectly classified as bubbles. TN (True Negatives) refers to the number of semantic entities correctly classified as non-bubbles. Lastly, FN (False Negatives) represents the number of semantic entities wrongly classified as non-bubbles. Knowing these metrics, it is possible to calculate evaluation metrics such as accuracy, precision, recall, and F1 score.

Accuracy

Accuracy indicates the percentage of cases in which the model's predictions are correct out of the total number of cases evaluated (Eq. 10).

$$Accuracy = \frac{TP+TN}{TP+TN+FP+FN} \tag{10}$$

Evaluating models only based on accuracy can be problematic, especially when dealing with imbalanced ground truth components. High accuracy does not necessarily indicate effective model performance and can be misleading.

Recall

Recall, referred to as the true positive rate, measures the probability of correctly detecting ground truth objects (Eq. 11). For instance, a recall value of 0.9 tells that there is an 90% chance that the model accurately identifies the relevant objects out of the total number of ground truth objects.

$$Recall/sensibility = \frac{TP}{TP+FN} \text{ or } \frac{True\ Positive}{Actual\ Results} \tag{11}$$

Precision

Precision the proportion of true positive results among all instances predicted as positive. (Eq. 12). Like recall, precision scores also fall within the range of 0 to 1. For example, a precision value of 0.75 indicates that when the model detects an object, it is correct 75% of the time.

$$Precision = \frac{TP}{TP+FP} \text{ or } \frac{True\ Positive}{Predictive\ Results} \tag{12}$$

F1- score

The F1 score takes into account both recall and precision metrics to calculate its value. It is calculated as the harmonic mean of these two metrics (Eq. 13), and ranges from 0 to 1. In other words, the F1 score provides a comprehensive assessment of the model's performance by considering both the model's ability to correctly identify relevant instances (recall) and the accuracy of those identifications (precision).

$$F1 = \frac{2 \times Recall \times Precision}{Recall \times Precision} \tag{13}$$

4. DATA ACQUISITION

As part of this master thesis project, a total of 15,795 images depicting oxygen bubbles were collected by the experimental team led by Dr. Rodenbuecher at the Juelich research center, IEK-14.

In the electrolysis mode of a reversible PEM fuel cell, operating at a voltage of 1.5V, a standard camera captured images at the anodic side (Fig. 2.15). These images have a resolution of 640 × 630 pixels and were recorded with an interval of 33 milliseconds. The electrolysis experiment was conducted under standard conditions of room temperature (25°C) and atmospheric pressure of 1 atm.

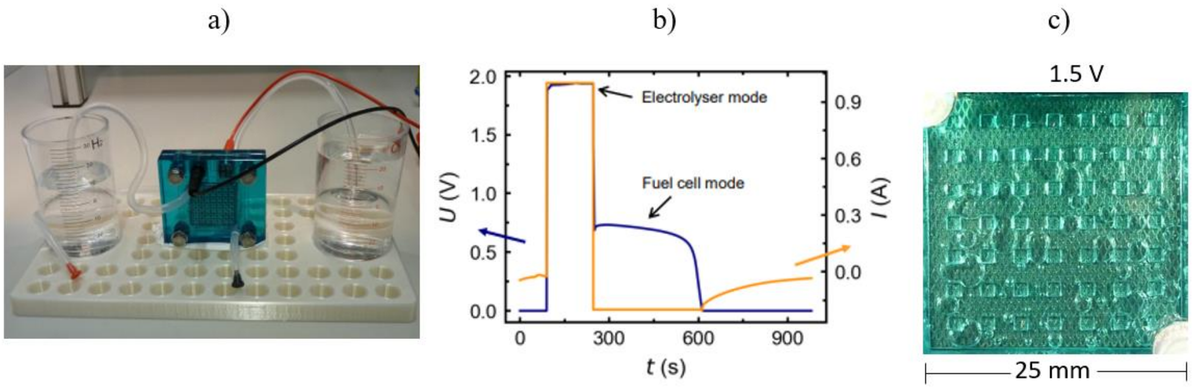

Fig. 2.15. a) reversible fuel cell experimental setup, b) polarization curves in electrolyzer and fuel cell modes, and c) oxygen bubble image at 1.5 V.

5. EXPERIMENTAL PART

The approach employed in this project to enable automated image analysis of oxygen bubbles at the anode side of PEM water electrolyzers is structured into four primary steps, as visually represented in the developed software pipeline in Fig. 2.16. The basis of this image analysis relies on evaluating the distribution of oxygen bubble areas on the anodic plate.

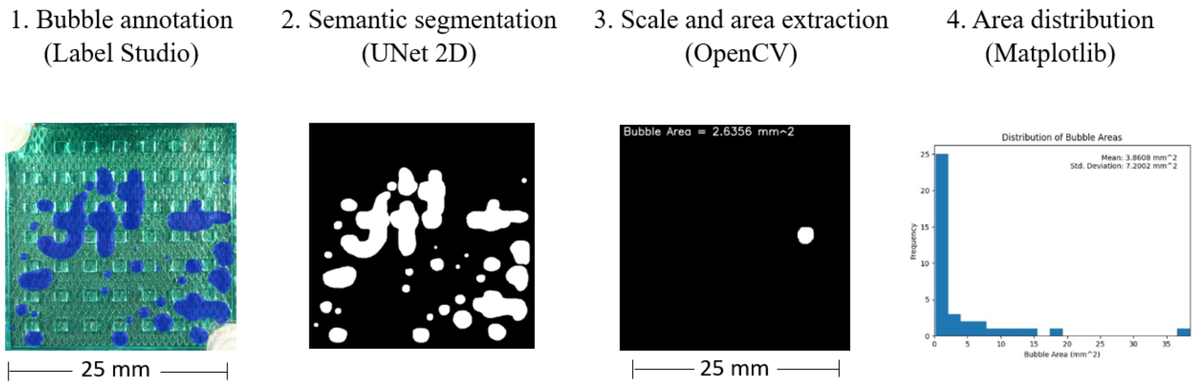

Fig. 2.16. Methodical pipeline illustration of the automated bubble image analysis.

1. bubble annotation using Label Studio, 2. model training for bubble semantic segmentation via UNet 2D, 3. Calibration followed by individual bubble area extraction using OpenCV, 4. Lastly, distribution of the extracted bubble areas via Matplotlib library.

5.1 Dataset Annotation and preprocessing

The annotation of data represents the first step and delicate task to efficiently train a deep learning model. Data annotation consists of manually assigning labels to the objects of interest or regions of interests (ROIs) inside the data for training purpose, enabling the model to predict on unseen data having relatively the same patterns or features. It is crucial to execute the data annotation process with precision to avoid incorrect labeling, which can cause confusion for the model being trained and ultimately lead to a poor performance of the model. Moreover, the process of data annotation, being a manual and precision-driven task, requires more time to be completed.

To carry out the annotation of the bubble images, we employed the use of "Label Studio" version 1.8.0, an advanced open-source annotation software that offers a user-friendly interface (Fig. 2.17). This software simplifies the manual annotation task and facilitates the data management.

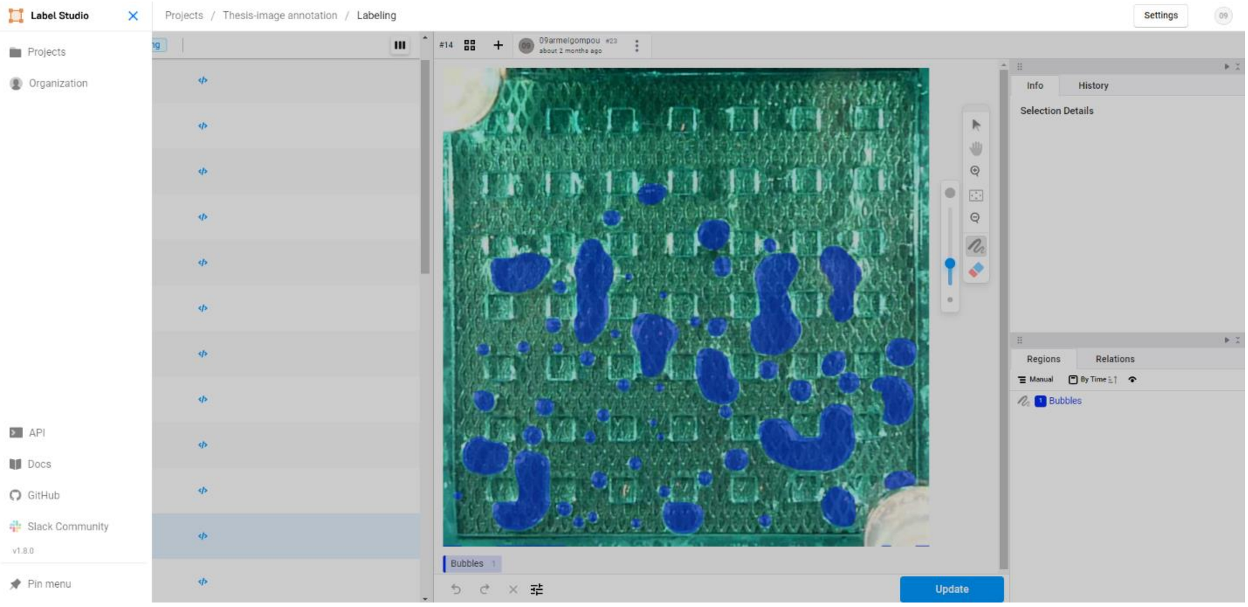

Fig. 2.17. Illustration of Label Studio interface.

A set of 35 images, each having a resolution of 640 × 630 pixels and a scale of 25 mm, were annotated. Emphasis was placed on bubbles exhibiting complex shapes and a high degree of blurriness to minimize the chances of overlooking the bubbles or inaccurately annotating them.

After performing the manual annotation task, the original bubble images used for the annotation, along with their resultant masks were pre-processed to be conformed to the data type specifications of the UNet 2D model used in this project. The original bubble images were converted to grayscale, resized to dimensions of 512 × 512 pixels, and saved in "tif format". Similarly, the masks associated with these were binarized with pixel values of 0 and 255, resized to 512 × 512 pixels, and saved in "tif format" as well.

5.2. Semantic Segmentation Model Training

A UNet (2D) model was trained from scratch for 150 epochs on 28 paired image patches (image dimensions: (512, 512), patch size: (512,512)) with a batch size of 4 and a weighted binary crossentropy loss function, using the U-Net (2D) ZeroCostDL4Mic notebook (version 2) [66]. The dataset was augmented by applying rotation, random zoom magnification, and shifting. The training was completed in 19 minutes 10 seconds, and was accelerated using a Tesla T4 GPU provided by Google. Table 2.2 shows the parameters used for training.

Table 2.2. UNet (2D) training parameters and their corresponding values

Parameter	value
number of epochs	150
patch size	512 × 512
batch size	4
number of steps	7
percentage validation	10
initial learning rate	0.0001
pooling steps	3
minimum fraction	0.02

Number of epochs: represent the total number of complete cycles of forward and backward propagation that the model undergoes during training on the training set.

Patch size: refer to the specified width and height of rectangular or square regions used for analysis within an image. It determines the size of the areas considered for localized processing or feature extraction.

Batch size: refer to the number of images that are loaded into the network per step. Smaller batch sizes may improve training performance slightly but may increase training time.

Number of steps: correspond to the number of images in the training set divided by the batch size.

Percentage Validation: indicate the percentage of images selected from the training set that is allocated for validation during the training process.

Initial learning rate: correspond to the value set at the start of the training process, which signifies the speed at which the model learns.

Pooling steps: refer to the stride or step size used in the pooling operation, determining the amount of displacement between neighboring pooling regions during downsampling (contraction path).

Minimum fraction: refer to the smallest proportion of foreground pixels required within a chosen patch for it to be considered as a valid patch.

5.3. Model Evaluation: Quality Control

To assess the effectiveness of the trained UNet (2D) model for semantic image segmentation, an unseen dataset consisting of 7 image pairs was generated. Each pair includes a raw image and its corresponding ground truth mask. The trained model is applied to these images, generating predicted masks. The evaluation process involves measuring the Intersection over Union (IoU) metric for each predicted mask at various threshold values ranging from 0 to 255. Furthermore, a confusion matrix is constructed to categorize the predicted pixels as true positives (TP), false positives (FP), true negatives (TN), and false negatives (FN). These metrics are then utilized to compute the recall, precision, and F1-score, providing insights into the model's performance.

5.4. Computer Vision-Based Bubble Area Extraction

Computer Vision is a scientific field that involves programming computers to process and comprehend images and videos [67]

We employed the use of OpenCV, an open-source computer vision library, to extract individual bubbles from a mask and accurately calculate their respective areas. To determine the area of a bubble, we made use of the cv2.findContours() function to detect its contour, followed by the application of the cv2.contourArea() function. The calculated area is then calibrated to the original scale, which is 25 mm, with a resolution of 640 × 630 pixels.

5.5. Bubble Area Distribution

To analyze the distribution of bubble areas in individual image, we utilized Matplotlib, a Python library for 2D and 3D data visualization. Matplotlib enables the creation of high-quality figures suitable for scientific publications and interactive environments across different platforms [68]. By employing Matplotlib, we were able to visualize the bubble area distribution through histograms, as well as extract important statistical metrics such as the mean area and standard deviation.

PARTIAL CONCLUSION

Deep Learning is subfield of machine learning (with machine learning which is part of the broader domain of artificial intelligence) that mimics the human brain’s neural networks to process data. The data processing is executed through a trained artificial neural network which is a UNet (2D) model in this present study. Furthermore, to enable automated image analysis of oxygen bubbles at the anode side of PEM water electrolyzers, a methodological pipeline was developed and structured into four primary steps: 1. bubble annotation using Label Studio, 2. model training for bubble semantic segmentation via UNet 2D, 3. Calibration followed by individual bubble area extraction using OpenCV, 4. Lastly, distribution of the extracted bubble areas via Matplotlib library.

CHAPTER 3: RESULTS AND DISCUSSION

CHAPTER 3: RESULTS AND DISCUSSION

In this chapter, we present and discuss the findings achieved at every stage of our methodological approach.

1. DATASET ANNOTATION

The process of manual annotation using Label Studio (version 1.8.0) involved meticulously labeling the bubbles present within the 35 images selected for this task, creating a comprehensible dataset for training the UNet model and assessing the quality of the model's prediction. During the annotation phase, review sessions were conducted to address any ambiguities or uncertainties, ensuring the accuracy and consistency of the annotations. The annotation process results are depicted in Fig. 3.1, showcasing three representative examples.

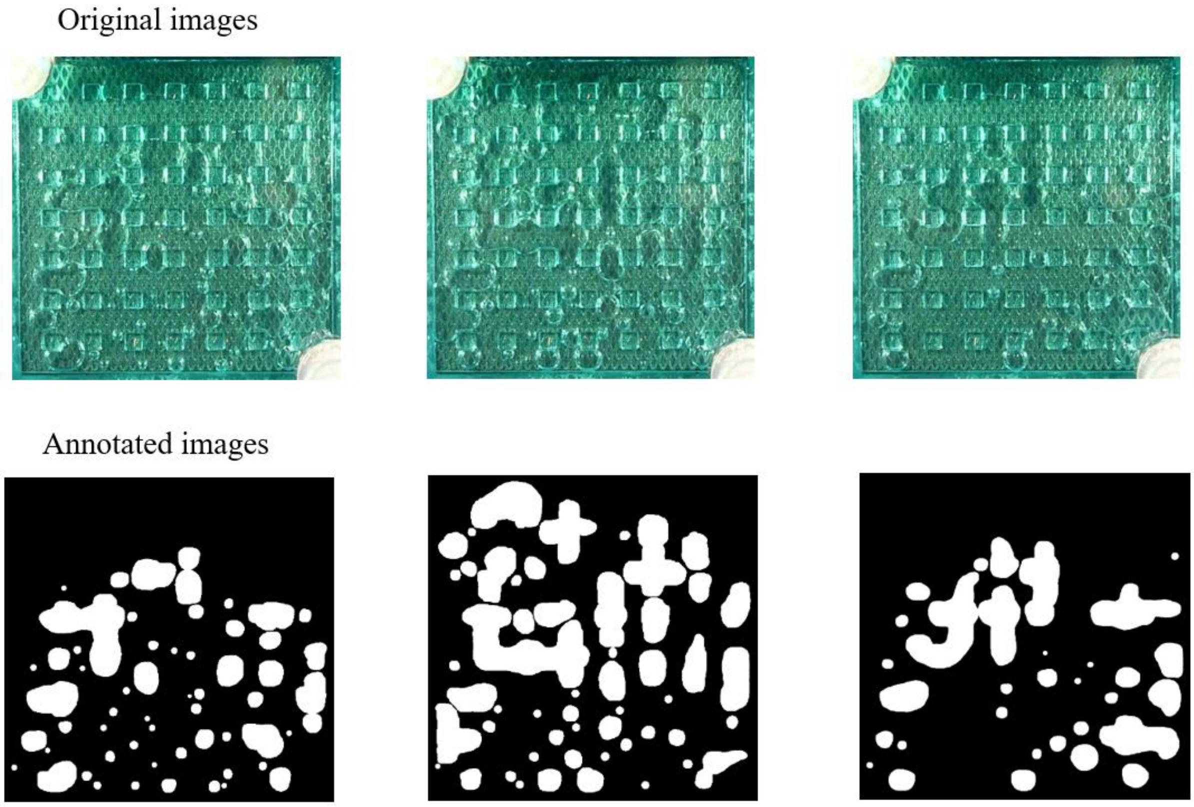

Fig. 3.1. Illustration of the resulting annotated images obtained from their corresponding original images using Label Studio.

In the annotated images, the bubbles (ROIs) are represented by the color white, with a corresponding pixel value of 255. On the other hand, the background is depicted in black with a pixel value of 0. However, a limitation arises in Label studio when saving the annotated images, as the border of labeled bubbles exhibits varying pixel values (ranging from 1 to 255), which fails to clearly define the border of these bubbles. To address this, a binarization process is applied to the images using a threshold value of 127, ensuring a well-defined border.

2. SEMANTIC SEGMENTATION MODEL TRAINING

The training from scratch of the UNet (2D) model on a dataset of 28 paired images (on which was applied data augmentation techniques) was performed with a computational power of a Tesla T4 GPU. After 150 epochs, the training process was concluded within a time frame of 19 minutes and 10 seconds, resulting in the generation of two plots showing the evolution of the training loss as well as the validation loss (Fig. 3.2).

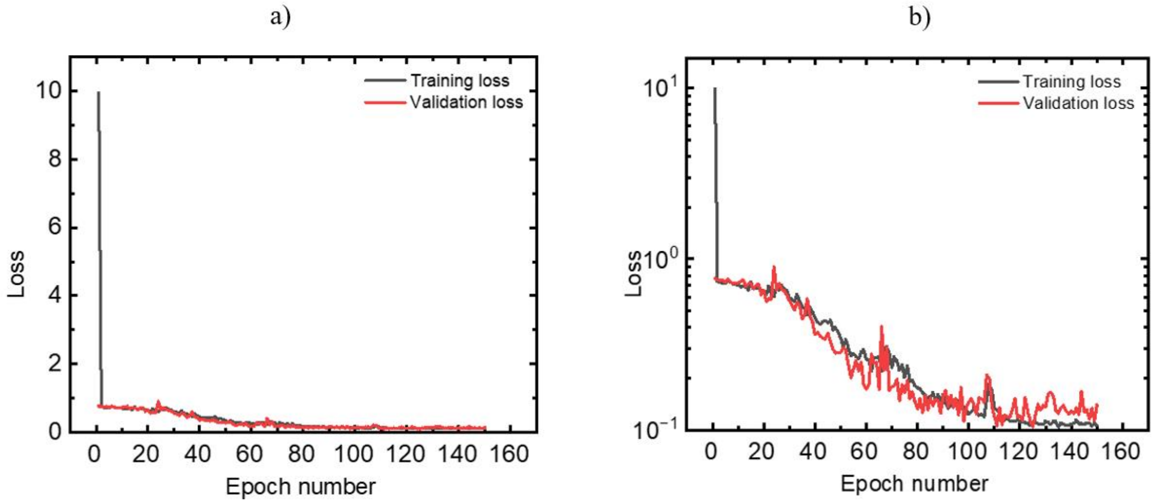

Fig. 3.2. Training loss (black curve) and validation loss (red curve) curves at a) linear scale, and b) logarithmic scale.

Training loss refers to the measure of error between the model’s prediction on the training image and its actual ground-truth, which is calculated after each epoch. While, Validation loss refers to the measure of error between the model's prediction on a validation image and the corresponding ground-truth, which is also calculated after each epoch. A model's performance is considered better when both the training loss and validation loss values approach zero.

Both plots depict identical evolution of the training loss and validation loss over the epochs, but represented at different scale. Plot (a) adopts a linear scale, which allows for a clearer visualization of how closely these curves approach zero. On the other hand, plot (b) employs a logarithmic scale, which helps highlight the subtle variations between the training loss and validation loss, making it easier to discern small differences between the two.

The training loss and validation loss demonstrate a noticeable overall decrease, both indicating approximatively the same downward trends over the observed epochs. However, within these downward trends, there are intermittent fluctuations where the training loss and validation loss curves exhibit a periodic upward and downward movements (zig-zag tendency). The similarity in the trends of the training loss and validation loss (training loss and validation loss being close to each other) indicates that the trained UNet (2D) model is not overfitted. Furthermore, the convergence towards zero (0.11 for training loss and 0.14 for validation loss at epoch 150) demonstrates the good performance of the model.

At the end of the training process, the UNet (2D) model is saved at two different epochs. Firstly, at epoch number 150, which is the final epoch. At this stage, the model has a training loss value of 0.11 and a validation loss value of 0.14. Secondly at epoch number 125, where the model demonstrates its best performance. At this epoch, the model achieves a training loss value of 0.11 and a validation loss value of 0.10, corresponding to the best weights obtained in the entire training process. Thus, the considered trained UNet (2D) model is the one recorded at the epoch 125 since it offers the best weight values.

3. MODEL EVALUATION: QUALITY CONTROL

The application of the trained UNet (2D) model on the 7 unseen raw images (inputs) gives 7 prediction masks which are not binarized yet. These prediction masks are overlaid on their corresponding ground-truth masks to determine the IoU value of each predicted image, considering threshold values varying from 0 to 255, as illustrated in Fig. 3.3.

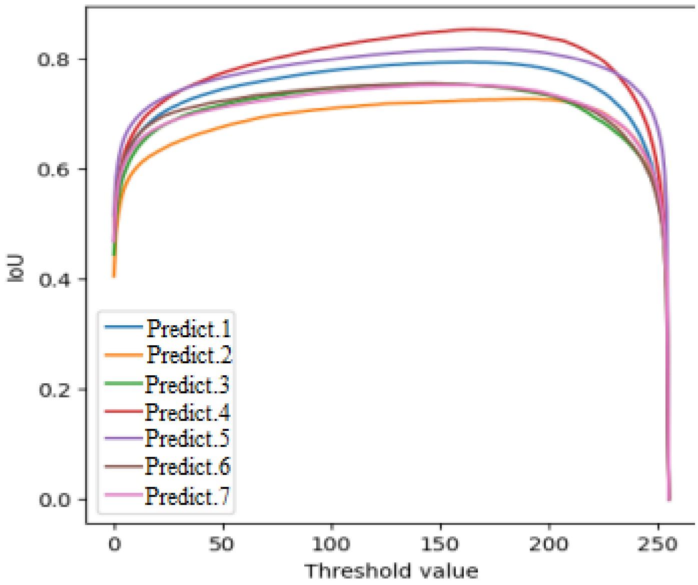

Fig. 3.3. Determination of the IoU of each prediction mask in function of different threshold values.

For each prediction mask, corresponds a best IoU obtained at an optimum threshold value, as shown in table 3.1.

Table 3.1. Value of the IoU of each prediction mask and its corresponding IoU-optimized binary threshold value.

Prediction mask	IoU	IoU-optimized threshold
prediction 1	0.794	162
prediction 2	0.727	192
prediction 3	0.754	137
prediction 4	0.854	165
prediction 5	0.819	168
prediction 6	0.755	145
prediction 7	0.752	160

By examining the table, we can see that the IoU values are predominantly close to 1, suggesting that the model's predictions are accurate. Fig. 3.4 presents a visual representation of the quality control process for a single image (prediction 1).

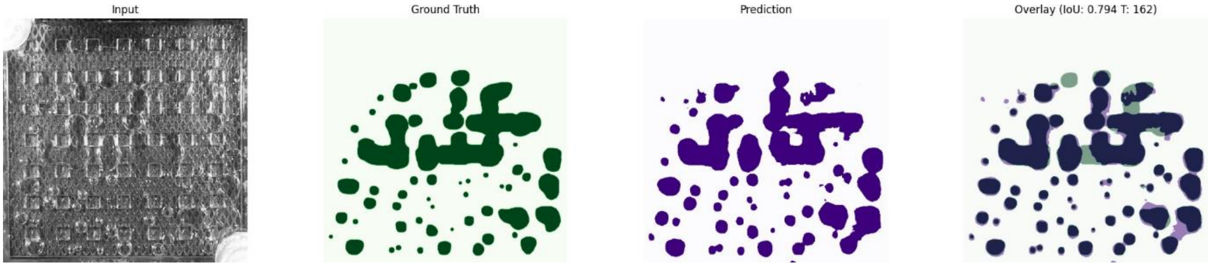

Fig. 3.4. Quality control visualization corresponding to prediction 1. The input is passed through the trained model, resulting in a prediction that is overlaid on the ground-truth.

We notice (in Fig.3.4) that while the trained UNet (2D) model successfully predicts the majority of bubbles accurately there are a few instances where some bubbles appear slightly larger in size, merged, and have rougher borders compared to the ground-truth. Additionally, there are cases where the model predicts bubbles that do not exist in the ground-truth (FP), as well as missing the prediction of some bubbles that are present in the ground-truth (FN).

Furthermore, this trained model struggles to accurately predict the intersections of the bubbles, resulting in numerous partial and inaccurate intersections, as also demonstrated by Hessenkemper *et al.* [69]. These prediction defects highlight the limitation of the model.

By categorizing the prediction pixels according to the ground-truth pixels, the confusion matrix displayed in Table 3.2 is obtained. The categorization includes the 7 prediction masks.

Table 3.2. Confusion matrix of bubble pixels identification.

		Actual Value	
		Bubbles Pixels	Non-bubbles Pixels
Predicted Value	Bubble Pixels	331,616 (TP)	73,227 (FP)
	Non-bubbles Pixels	37,792 (FN)	1,392,373 (TN)

The determination of TP, TN, FP, and FN values allowed for the computation of recall, precision, and F1-score. The resulting metrics revealed a recall of 0.89, indicating that the trained model correctly identifies 89% of the actual bubbles out of the total ground-truth bubbles, a precision of 0.81, signifying 81% of the time, the actual bubble is accurately identified, and an F1-score of 0.85, demonstrating a balanced measure of both precision and recall and which indicates a relatively good overall performance of the trained model.

4. BUBBLE AREA EXTRACTION

OpenCV2 enables the extraction of the bubble areas by isolating individually the bubbles. Fig. 3.5 illustrates the results of the isolation of two bubbles, and indicates their corresponding areas.

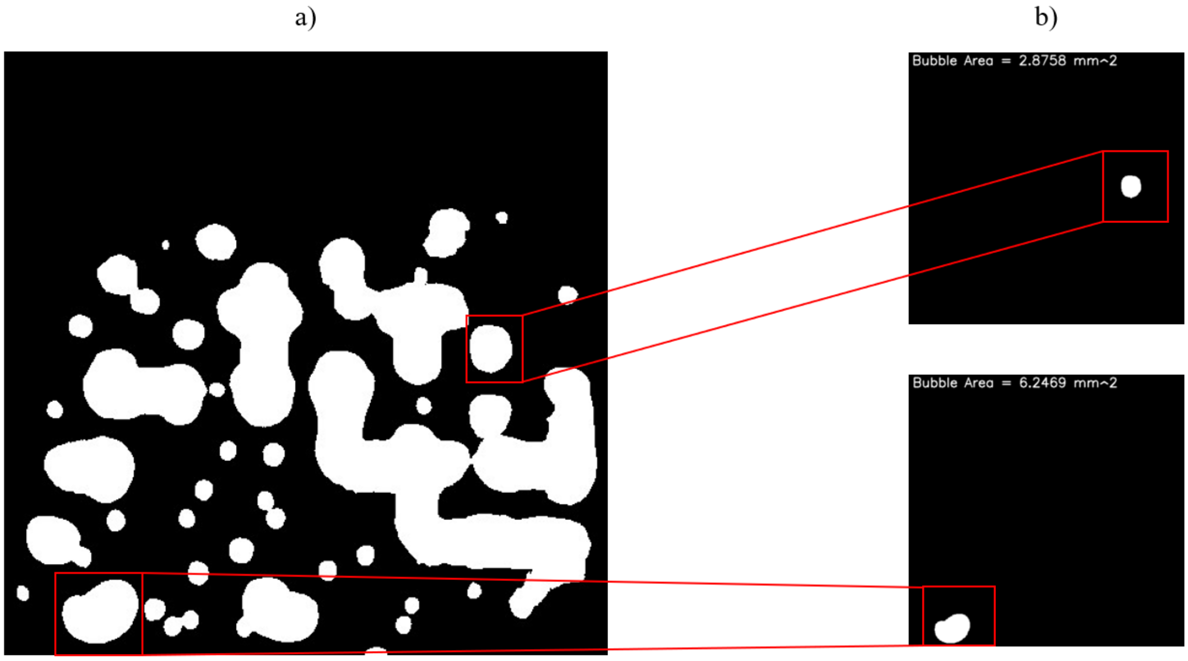

Fig. 3.5. Illustration of bubble area extraction using OpenCV2. a) Obtained segmentation mask after prediction with the UNet (2D) model and binarization. b) Computer vision-driven bubble area extraction after resizing and calibration.

The total area of bubbles was determined for each of the predicted images (predicted masks), as well as their corresponding manual annotated images (ground-truth masks). These calculations were conducted to enable a comparative analysis. The results of these computations are summarized in Fig. 3.6.

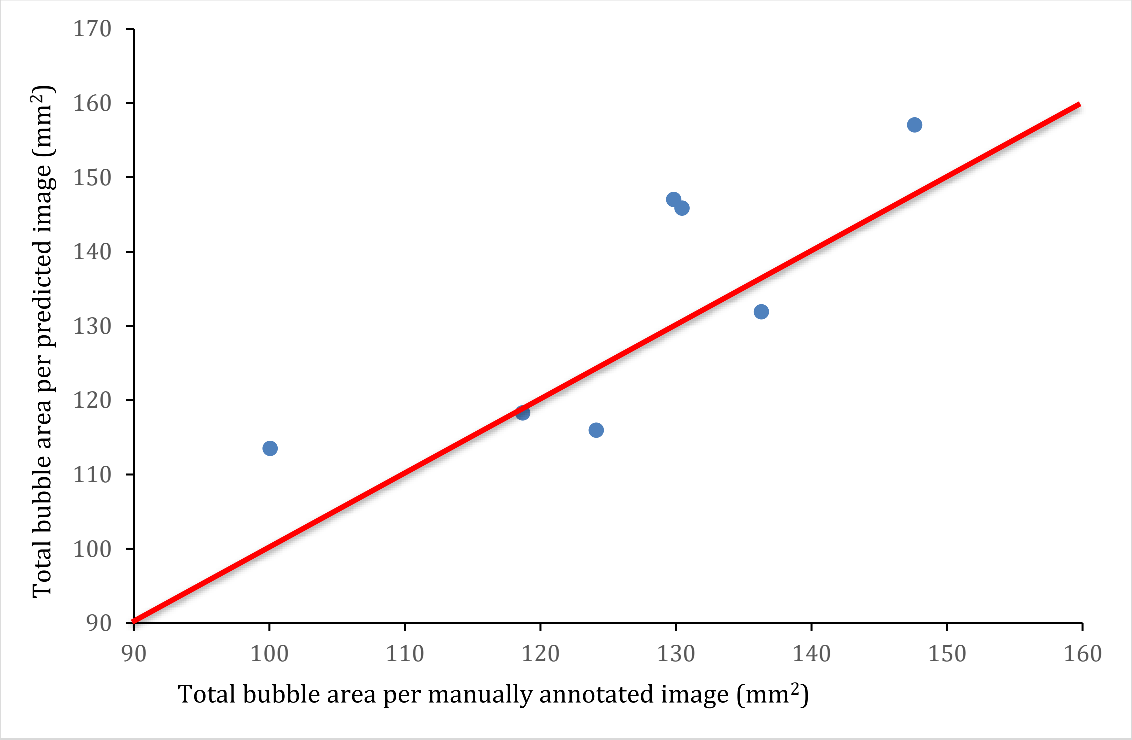

Fig. 3.6. Polydispersity plot comparing the total bubble area of each manual annotated image and their associated predicted image.

The comparison reveals a smaller disparity in the overall bubble area between the manually annotated images and their corresponding predicted images, providing further evidence of the model's achieved performance values.

5. BUBBLE AREA DISTRIBUTION

After utilizing OpenCV2 to extract the bubble areas from individual images, Matplotlib is employed to analyze their distribution. The obtained results, including the average area and standard deviation, are visualized in fig. 3.7. This figure illustrates the bubble area distribution for 3 predicted images.

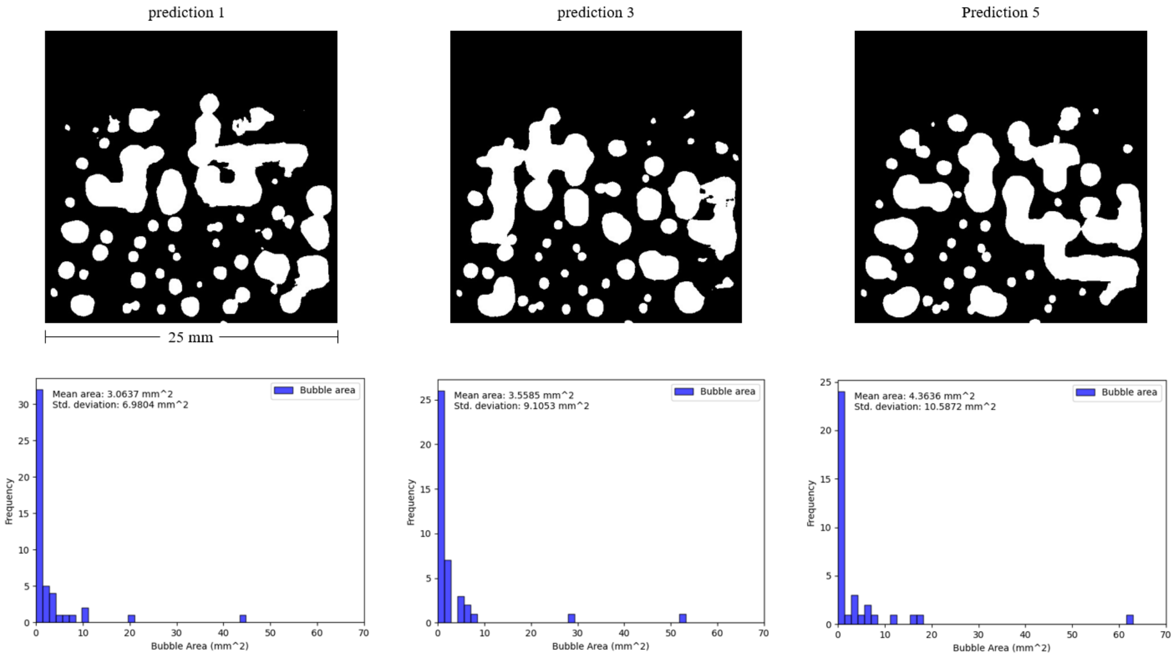

Fig. 3.7. Illustration of 3 predicted images at a 25 mm scale, along with their corresponding histograms showing the distribution of bubble areas, the mean area, and the standard deviation.

The mean bubble area obtained from each predicted image offers a central measure that represents the typical area of bubbles in those images. This information allows us to understand the overall scale of bubbles present in each predicted. A higher mean area suggests the prevalence of larger bubbles. Conversely, a lower average area indicates the dominance of smaller bubbles. For instance in prediction 1 (fig. 3.6), the mean bubble area of 3.06 mm^2 indicates that, on average, the predicted image contain bubbles with an area of approximately 3.06 mm^2.

Futhermore, The standard deviation of bubble areas provides essential information about the spread or dispersion of bubble sizes. A larger standard deviation suggests a wide range of bubble areas, indicating a diverse distribution. This could arise from various factors influencing bubble formation and growth, resulting in bubbles of different areas. On the other hand, a smaller standard deviation implies a more tightly clustered distribution of bubble areas, indicating a more uniform bubble population in the predicted image. The example in prediction 1 (fig. 3.2) depicts a standard deviation of 6.98 mm^2. This means that, on average, individual bubble areas in the predicted image differ from the mean area (3.06 mm^2) by approximately 6.98 mm^2.

PARTIAL CONCLUSION

UNet (2D) model was trained and evaluated on a total of 35 images (28 images for model training and 7 images for model evaluation) which were firstly manually annotated using Label Studio. The trained UNet model showed a relatively good performance: a recall of 0.89, a precision of 0.81, and a F1-score of 0.85 depicting how well the model is able to predict on data that have not been seen before. Moreover, the statistical distribution analysis conducted on the predicted bubbles after being extracted from the prediction images, revealed a dominant presence of small bubbles with only a slight variation in standard deviation.

GENERAL CONCLUSION AND PERSPERCTIVES

GENERAL CONCLUSION AND PERSPECTIVES

The application of deep learning technique to automate image analysis of oxygen bubble dynamics in PEM electrolyzers marks a significant milestone in the field of renewable energy research. Throughout this study, we have demonstrated the potential of harnessing cutting-edge deep learning and computer vision algorithms to unlock valuable insights into the area distribution of oxygen bubbles on the anodic plate of a PEM water electrolyzer under a voltage of 1.5 V.

In our approach to perform automated image analysis of oxygen bubbles, we developped a multi-step pipeline from the bubble image to the bubble area distribution as followed: 1. manual annotation of 35 oxygen bubble images with label studio as dataset for training and model quality control, 2. training of UNet (2D) model on 28 annotated data for semantic segmentation of bubbles, 3. individual bubble area measurements using a computer vision algoritm, and finally 4. statistical distribution of bubble areas using matplotlib library.

Despite the small number of training data, and the complexity of the bubbles‘ shapes, the results of our deep learning model training exhibit good performance, as indicated by a recall of 0.89, precision of 0.81, and an F1-score of 0.85. Moreover, the approximate area similarities between the predicted and actual images demonstrate the model's robustness. Additionally, when evaluating at 1.5 V, we observed a dominant presence of small bubbles with only a slight variation in standard deviation.

While the results of our study are indeed promising, we acknowledge that there is still room for improvement. As the field of deep learning continues to evolve, integrating novel neural network architecture and exploring diverse data augmentation techniques could enhance the model's performance even further.

The future work, extending beyond the scope of this master thesis study, will focus on the following aspects: firstly, training of a more advanced model, like YOLO-V8, to carry out real-time instance segmentation in videos captured at various cell voltages. Secondly, real-time extraction and statistical analysis of bubble parameters, including area, diameter, aspect ratio, solidity, orientation, extent, perimeter, and roundness. lastly, establishing correlations between these extracted parameters and validating them against the physical model.

REFERENCES

1. D. Gautam & N. B. Bolia, Air pollution: impact and interventions. *Air Quality, Atmosphere and Health*, **13** (2020) 209–223. https://doi.org/10.1007/s11869-019-00784-8.
2. R. Sivarethinamohan, S. Sujatha, S. Priya, Sankaran, A. Gafoor, & Z. Rahman, Impact of air pollution in health and socio-economic aspects: Review on future approach. *Mater Today Proc* (Elsevier Ltd, 2020), pp. 2725–2729. https://doi.org/10.1016/j.matpr.2020.08.540.
3. S. A. Raza, N. Shah, & A. Sharif, Time frequency relationship between energy consumption, economic growth and environmental degradation in the United States: Evidence from transportation sector. *Energy*, **173** (2019) 706–720. https://doi.org/10.1016/j.energy.2019.01.077.
4. M. S. Alam, T. A. Chowdhury, A. Dhar, F. S. Al-Ismail, M. S. H. Choudhury, M. Shafiullah, M. I. Hossain, M. A. Hossain, A. Ullah, & S. M. Rahman, Solar and Wind Energy Integrated System Frequency Control: A Critical Review on Recent Developments. *Energies*, **16** (2023) 812. https://doi.org/10.3390/en16020812.
5. A. K. Sarker, A. K. Azad, M. G. Rasul, & A. T. Doppalapudi, Prospect of Green Hydrogen Generation from Hybrid Renewable Energy Sources: A Review. *Energies*, **16** (2023) 1556. https://doi.org/10.3390/en16031556.
6. A. Majumdar, M. Haas, I. Elliot, & S. Nazari, Control and control-oriented modeling of PEM water electrolyzers: A review. *International Journal of Hydrogen Energy*, (2023) ISSN 0360-3199. https://doi.org/10.1016/J.IJHYDENE.2023.04.204.
7. S. Yuan, C. Zhao, X. Cai, L. An, S. Shen, X. Yan, & J. Zhang, Bubble evolution and transport in PEM water electrolysis: Mechanism, impact, and management. *Progress in Energy and Combustion Science*, **96** (2023) 101075. https://doi.org/10.1016/J.PECS.2023.101075.
8. E. Leonard, A. D. Shum, S. Normile, D. C. Sabarirajan, D. G. Yared, X. Xiao, & I. V. Zenyuk, Operando X-ray tomography and sub-second radiography for characterizing transport in polymer electrolyte membrane electrolyzer. *Electrochimica Acta*, **276** (2018) 424–433. https://doi.org/10.1016/j.electacta.2018.04.144.
9. A. Colliard-Granero, M. Batool, J. Jankovic, J. Jitsev, M. H. Eikerling, K. Malek, & M. J. Eslamibidgoli, Deep learning for the automation of particle analysis in catalyst layers for polymer electrolyte fuel cells. *Nanoscale*, **14** (2022) 10–18. https://doi.org/10.1039/d1nr06435e.

10. M. Carmo, D. L. Fritz, J. Mergel, & D. Stolten, A comprehensive review on PEM water electrolysis. *International Journal of Hydrogen Energy*, **38** (2013) 4901–4934. https://doi.org/10.1016/j.ijhydene.2013.01.151.

11. L. J. Nuttall, A. P. Fickett, & W. A. Titterington, Hydrogen Generation by Solid Polymer Electrolyte Water Electrolysis. *Hydrogen Energy*, (1975) 441-455.

12. K. Onda, T. Murakami, T. Hikosaka, M. Kobayashi, R. Notu, & K. Ito, Performance Analysis of Polymer-Electrolyte Water Electrolysis Cell at a Small-Unit Test Cell and Performance Prediction of Large Stacked Cell. *Journal of The Electrochemical Society*, **149** (2002) A1069. https://doi.org/10.1149/1.1492287.

13. R. Lin, Y. Lu, J. Xu, J. Huo, & X. Cai, Investigation on performance of proton exchange membrane electrolyzer with different flow field structures. *Applied Energy*, **326** (2022) 120011. https://doi.org/10.1016/J.APENERGY.2022.120011.

14. iea, 2022. Electrolysers – Analysis. [online]. Available on: https://www.iea.org/reports/electrolysers. Accessed June 5th, 2023.

15. K. Zhang, X. Liang, L. Wang, K. Sun, Y. Wang, Z. Xie, Q. Wu, X. Bai, M. S. Hamdy, H. Chen, & X. Zou, Status and perspectives of key materials for PEM electrolyzer. *Nano Research Energy*, **1** (2022) e9120032. https://doi.org/10.26599/nre.2022.9120032.

16. *WIKIPEDIA, 2013. PEM electrolysis loss breakdown*. [online]. Available on: https://en.wikipedia.org/wiki/File:PEM_electrolysis_loss_breakdown.pdf. Accessed July 19th, 2023.

17. A. S. Tijani, N. A. Binti Kamarudin, & F. A. Binti Mazlan, Investigation of the effect of charge transfer coefficient (CTC) on the operating voltage of polymer electrolyte membrane (PEM) electrolyzer. *International Journal of Hydrogen Energy*, **43** (2018) 9119–9132. https://doi.org/10.1016/j.ijhydene.2018.03.111.

18. S. Toghyani, S. Fakhradini, E. Afshari, E. Baniasadi, M. Y. Abdollahzadeh Jamalabadi, & M. Safdari Shadloo, Optimization of operating parameters of a polymer exchange membrane electrolyzer. *International Journal of Hydrogen Energy*, **44** (2019) 6403–6414. https://doi.org/10.1016/j.ijhydene.2019.01.186.

19. X. Sun, K. Xu, C. Fleischer, X. Liu, M. Grandcolas, R. Strandbakke, T. S. Bjørheim, T. Norby, & A. Chatzitakis, Earth-abundant electrocatalysts in proton exchange membrane electrolyzers. *Catalysts*, **8** (2018) 657. https://doi.org/10.3390/catal8120657.

20. K. W. Ahmed, M. J. Jang, M. G. Park, Z. Chen, & M. Fowler, Effect of Components and Operating Conditions on the Performance of PEM Electrolyzers: A Review. *Electrochem*, **3** (2022) 581–612. https://doi.org/10.3390/electrochem3040040.

21. H. Teuku, I. Alshami, J. Goh, M. S. Masdar, & K. S. Loh, Review on bipolar plates for low-temperature polymer electrolyte membrane water electrolyzer. *International Journal of Energy Research*, **45** (2021) 20583–20600. https://doi.org/10.1002/er.7182.

22. X. Lin, J. Z. Y. Seow, & Z. J. Xu, A brief introduction of electrode fabrication for proton exchange membrane water electrolyzers. *JPhys Energy,* **5** (2023) 034003. https://doi.org/10.1088/2515-7655/acccb1.

23. O. Romiluyi, N. Danilovic, A. T. Bell, & A. Z. Weber, Membrane-electrode assembly design parameters for optimal CO_2 reduction. *Electrochemical Science Advances,* **3** (2023) e2100186. https://doi.org/10.1002/elsa.202100186.

24. X. Liu, J. Tian, C. Zhou, J. Jiang, X. Cheng, L. Yang, Q. Wu, X. Wang, & Z. Hu, Constructing membrane electrodes of low Pt areal loading with the new support of N-doped carbon nanocages for PEMFC. *FlatChem,* **40** (2023) 100515. https://doi.org/10.1016/J.FLATC.2023.100515.

25. J. Mo, Z. Kang, G. Yang, S. T. Retterer, D. A. Cullen, T. J. Toops, J. B. Green, & F. Y. Zhang, Thin liquid/gas diffusion layers for high-efficiency hydrogen production from water splitting. *Applied Energy,* **177** (2016) 817–822. https://doi.org/10.1016/j.apenergy.2016.05.154.

26. G. Athanasaki, A. Jayakumar, & A. M. Kannan, Gas diffusion layers for PEM fuel cells: Materials, properties and manufacturing – A review. *International Journal of Hydrogen Energy*, **48** (2023) 2294–2313. https://doi.org/10.1016/J.IJHYDENE.2022.10.058.

27. H. Nara, S. Tominaka, T. Momma, & T. Osaka, Impedance Analysis Counting Reaction Distribution on Degradation of Cathode Catalyst Layer in PEFCs. *Journal of The Electrochemical Society*, **158** (2011) B1184. https://doi.org/10.1149/1.3610988.

28. C. Rozain & P. Millet, Electrochemical characterization of Polymer Electrolyte Membrane Water Electrolysis Cells. *Electrochimica Acta*, **131** (2014) 160–167. https://doi.org/10.1016/j.electacta.2014.01.099.

29. D. K. Paul, J. B. Giorgi, & K. Karan, Chemical and Ionic Conductivity Degradation of Ultra-Thin Ionomer Film by X-ray Beam Exposure. *Journal of The Electrochemical Society,* **160** (2013) F464–F469. https://doi.org/10.1149/2.024306jes.

30. J. Manthey, M. Guesmi, R. Schab, S. Unz, & M. Beckmann, A sensitivity analysis on the bubble departure diameter for bubble growth due to oxygen super-saturation in highly purified water. *International Journal of Thermofluids,* **18** (2023) 100327. https://doi.org/10.1016/j.ijft.2023.100327.

31. A. Nouri-Khorasani, E. Tabu Ojong, T. Smolinka, & D. P. Wilkinson, Model of oxygen bubbles and performance impact in the porous transport layer of PEM water electrolysis cells.

International Journal of Hydrogen Energy, **42** (2017) 28665–28680. https://doi.org/10.1016/j.ijhydene.2017.09.167.

32. Y. Li, G. Yang, S. Yu, Z. Kang, J. Mo, B. Han, D. A. Talley, & F. Y. Zhang, In-situ investigation and modeling of electrochemical reactions with simultaneous oxygen and hydrogen microbubble evolutions in water electrolysis. *International Journal of Hydrogen Energy*, **44** (2019) 28283–28293. https://doi.org/10.1016/j.ijhydene.2019.09.044.

33. Z. Shi, J. Li, Y. Wang, S. Liu, J. Zhu, J. Yang, X. Wang, J. Ni, Z. Jiang, L. Zhang, Y. Wang, C. Liu, W. Xing, & J. Ge, Customized reaction route for ruthenium oxide towards stabilized water oxidation in high-performance PEM electrolyzers. *Nature Communications*, **14** (2023) 843-855. https://doi.org/10.1038/s41467-023-36380-9.

34. R. Ramachandran, T. W. Chen, P. Veerakumar, G. Anushya, S. M. Chen, R. Kannan, V. Mariyappan, S. Chitra, N. Ponmurugaraj, & M. Boominathan, Recent development and challenges in fuel cells and water electrolyzer reactions: an overview. *RSC Advances*, **12** (2022) 28227–28244. https://doi.org/10.1039/d2ra04853a.

35. A. S. Aricò, S. Siracusano, N. Briguglio, V. Baglio, A. Di Blasi, & V. Antonucci, Polymer electrolyte membrane water electrolysis: Status of technologies and potential applications in combination with renewable power sources. *J Appl Electrochem,* **43** (2013), pp. 107–118. https://doi.org/10.1007/s10800-012-0490-5.

36. J. Zhou, H. Johansen, N. Danilovic, I. V. Zenyuk, & A. Z. Weber, Multiscale Modeling of Multiphase Transport in PEM Water Electrolyzer. *ECS Meeting Abstracts*, **MA2019-01** (2019) 1143–1143. https://doi.org/10.1149/MA2019-01/22/1143.

37. A. R. Zeradjanin, P. Narangoda, I. Spanos, J. Masa, & R. Schlögl, How to minimise destabilising effect of gas bubbles on water splitting electrocatalysts? *Current Opinion in Electrochemistry*, **30** (2021) 100797. https://doi.org/10.1016/j.coelec.2021.100797.

38. E. T. Ojong, J. T. H. Kwan, A. Nouri-Khorasani, A. Bonakdarpour, D. P. Wilkinson, & T. Smolinka, Development of an experimentally validated semi-empirical fully-coupled performance model of a PEM electrolysis cell with a 3-D structured porous transport layer. *International Journal of Hydrogen Energy,* **42** (2017) 25831–25847. https://doi.org/10.1016/j.ijhydene.2017.08.183.

39. Á. Hernández-Gómez, V. Ramirez, & D. Guilbert, Investigation of PEM electrolyzer modeling: Electrical domain, efficiency, and specific energy consumption. *International Journal of Hydrogen Energy,* **45** (2020) 14625–14639. https://doi.org/10.1016/j.ijhydene.2020.03.195.

40. T. Kadyk, D. Bruce, & M. Eikerling, How to Enhance Gas Removal from Porous Electrodes? *Scientific Reports,* **6** (2016) 38780. https://doi.org/10.1038/srep38780.

41. Y. Li, Z. Kang, J. Mo, G. Yang, S. Yu, D. A. Talley, B. Han, & F. Y. Zhang, In-situ investigation of bubble dynamics and two-phase flow in proton exchange membrane electrolyzer cells. *International Journal of Hydrogen Energy,* **43** (2018) 11223–11233. https://doi.org/10.1016/j.ijhydene.2018.05.006.

42. C. M. Anderson, J. Klein, H. Rajakumar, C. D. Judge, & L. K. Béland, Automated Detection of Helium Bubbles in Irradiated X-750. *Ultramicroscopy,* **217** (2020) 113068. https://doi.org/10.1016/j.ultramic.2020.113068.

43. S. Sun, F. Xu, L. Cai, D. Salvato, F. Dilemma, L. Capriotti, M. Xian, T. Yao, & M. Xian, An Efficient Instance Segmentation Approach for Extracting Fission Gas Bubbles on U-10Zr Annular Fuel. *arXiv preprint arXiv,* **2302** (2023) 12833.

44. Y. Kim & H. Park, Deep learning-based automated and universal bubble detection and mask extraction in complex two-phase flows. *Scientific reports,* **11** (2021) 8940. https://doi.org/10.1038/s41598-021-88334-0.

45. R. Jacobs, P. Patki, M. J. Lynch, S. Chen, D. Morgan, & K. G. Field, Materials swelling revealed through automated semantic segmentation of cavities in electron microscopy images. *Scientific reports,* **13** (2023) 5178. https://doi.org/10.1038/s41598-023-32454-2.

46. K. R. Chowdhary, Fundamentals of artificial intelligence. *New Delhi: Springer India, (*2020) pp. 603-49. https://doi.org/10.1007/978-81-322-3972-7.

47. M. Khaleel, A. A. Ahmed, & A. Alsharif, Artificial Intelligence in Engineering. *Brilliance: Research of Artificial Intelligence,* **3** (2023) 32–42. https://doi.org/10.47709/brilliance.v3i1.2170.

48. S. J. Russell, Rationality and intelligence. *Artificial intelligence,* **94** (1997) 57-77.

49. J. García & F. Fernández, A Comprehensive Survey on Safe Reinforcement Learning. *Journal of Machine Learning Research,* **16** (2015) 1437-1480.

50. *Proceedings 2011 International Conference on Mechatronic Science, Electric Engineering, and Computer: August 19-22, 2011, Jilin, China.* (IEEE, 2011).

51. S. Ding, H. Li, C. Su, J. Yu, & F. Jin, Evolutionary artificial neural networks: A review. *Artificial Intelligence Review,* **39** (2013) 251–260. https://doi.org/10.1007/s10462-011-9270-6.

52. K. Shiruru, An Introduction to Artificial Neural Network. *International Journal of Advance Research and Innovative Ideas in Education,* 1 (2016) 27-30.

53. S. Silvestrini & M. Lavagna, Deep Learning and Artificial Neural Networks for Spacecraft Dynamics, Navigation and Control. *Drones*, 2022, **6** (2022) 270. https://doi.org/10.3390/drones6100270.

54. J. A. Nichols, H. W. Herbert Chan, & M. A. B. Baker, Machine learning: applications of artificial intelligence to imaging and diagnosis. *Biophysical Reviews*, **11** (2019) 111–118. https://doi.org/10.1007/s12551-018-0449-9.

55. A. Colliard-Granero, 2022. Autonomous Characterization of Functional Energy Materials with Artificial Intelligence. Master Thesis, Universität zu Köln, Germany, 63p.

56. M. M. Taye, Theoretical Understanding of Convolutional Neural Network: Concepts, Architectures, Applications, Future Directions. *Computation*, **11** (2023) 52. https://doi.org/10.3390/computation11030052.

57. L. Ajallouda, F. Z. Fagroud, A. Zellou, & E. H. Benlahmar, Automatic key phrases extraction: an overview of deep learning approaches. *Bulletin of Electrical Engineering and Informatics*, **12** (2023) 303–313. https://doi.org/10.11591/eei.v12i1.4130.

58. J. F. Carvalho De Araújo, 2022. MisInfoBot2: fight misinformation on social media. Master Thesis, Faculdade De Engenharia Da Universidade Do Porto (FEUP), Portugal, 43p.

59. Chinese Automation Congress 2015 Wuhan, Zhong guo zi dong hua xue hui, Chinese Automation Congress 2015.11.27-29 Wuhan, & CAC 2015.11.27-29 Wuhan, *Proceedings, 2015 Chinese Automation Congress 27-29 November, 2015, Wuhan, China*.

60. S. Ghosh, N. Das, I. Das, & U. Maulik, Understanding deep learning techniques for image segmentation. *ACM Computing Surveys*, **52** (2019) 73-107. https://doi.org/10.1145/3329784.

61. A. Garcia-Garcia, S. Orts-Escolano, S. Oprea, V. Villena-Martinez, & J. Garcia-Rodriguez, A Review on Deep Learning Techniques Applied to Semantic Segmentation. *arXiv preprint arXiv*,**1704** (2017) 06857. https://doi.org/10.48550/arXiv.1704.06857.

62. H. Lamba, 2019. Understanding Semantic Segmentation with UNET: A Salt Identification Case Study. [online]. Available on: https://towardsdatascience.com/understanding-semantic-segmentation-with-unet-6be4f42d4b47. Accessed July 3rd, 2023.

63. N. Navab, J. Hornegger, W. M. Wells, & A. F. Frangi, *LNCS 9351* - Medical Image Computing and Computer-Assisted Intervention – *MICCAI 2015* (2015).

64. H. Zunair & A. Ben Hamza, Sharp U-Net: Depthwise convolutional network for biomedical image segmentation. *Computers in Biology and Medicine*, **136** (2021). https://doi.org/10.1016/j.compbiomed.2021.104699.

65. Baeldung, 2023. Intersection Over Union for Object Detection. [online]. Available on: https://www.baeldung.com/cs/object-detection-intersection-vs-union. Accessed July 22nd, 2023.

66. L. von Chamier, R. F. Laine, J. Jukkala, C. Spahn, D. Krentzel, E. Nehme, M. Lerche, S. Hernández-Pérez, P. K. Mattila, E. Karinou, S. Holden, A. C. Solak, A. Krull, T. O. Buchholz, M. L. Jones, L. A. Royer, C. Leterrier, Y. Shechtman, F. Jug, M. Heilemann, G. Jacquemet, & R. Henriques, Democratising deep learning for microscopy with ZeroCostDL4Mic. *Nature Communications*, **12** (2021) 2276. https://doi.org/10.1038/s41467-021-22518-0.

67. I. Culjak, D. Abram, T. Pribanic, H. Dzapo, & M. Cifrek, A brief introduction to OpenCV. Proceedings of the 35th International Convention MIPRO, Opatija, Croatia, 2012, pp. 1725-1730.

68. M. Mahamat, S. A. Adeshina, T. Arreytambe, & Institute of Electrical and Electronics Engineers, Proceedings of the 11th International Conference on Electronics, Computer and Computation (ICECCO'14): International Conference, September 29-October 1, 2014: Abuja, Nigeria.

69. H. Hessenkemper, S. Starke, Y. Atassi, T. Ziegenhein, & D. Lucas, Bubble identification from images with machine learning methods. *International Journal of Multiphase Flow*, **155** (2022) 104169. https://doi.org/10.1016/j.ijmultiphaseflow.2022.104169.